Received 11 June; accepted 21 August 2001.

1. Segref, A. *et al.* Mex67p which is an essential factor for nuclear mRNA export binds to both poly(A)$^+$ RNA and nuclear pores. *EMBO J.* **16,** 3256–3271 (1997).
2. Sträßer, K. & Hurt, E. C. Yra1p, a conserved nuclear RNA binding protein, interacts directly with Mex67p and is required for mRNA export. *EMBO J.* **19,** 410–420 (2000).
3. Libri, D., Graziani, N., Saguez, C. & Boulay, J. Multiple roles for the yeast *SUB2/yUAP56* gene in splicing. *Genes Dev.* **15,** 36–41 (2001).
4. Zhang, M. & Green, M. R. Identification and characterization of yUAP/Sub2p, a yeast homolog of the essential human pre-mRNA splicing factor hUAP56. *Genes Dev.* **15,** 30–35 (2001).
5. Kistler, A. L. & Guthrie, C. Deletion of MUD2, the yeast homolog of U2AF65, can bypass the requirement for Sub2, an essential spliceosomal ATPase. *Genes Dev.* **15,** 42–49 (2001).
6. Portman, D. S., O'Connor, J. P. & Dreyfuss, G. Yra1, an essential *Saccharomyces cerevisiae* gene, encodes a novel nuclear protein with RNA annealing activity. *RNA* **3,** 527–537 (1997).
7. Hurt, E. *et al.* Mex67p mediates the nuclear export of a variety of pol II transcripts. *J. Biol. Chem.* **275,** 8361–8368 (2000).
8. Jensen, T. H., Patricio, K., McCarthy, T. & Rosbash, M. A block to mRNA nuclear export in *S. cerevisiae* leads to hyperadenylation of transcripts that accumulate at the site of transcription. *Mol. Cell* **7,** 887–898 (2001).
9. Bousquet-Antonelli, C., Presutti, C. & Tollervey, D. Identification of a regulated pathway for nuclear pre-mRNA turnover. *Cell* **102,** 765–775 (2000).
10. Stutz, F. *et al.* REF, an evolutionarily conserved family of hnRNP-like proteins, interacts with TAP/Mex67p and participates in mRNA nuclear export. *RNA* **6,** 638–650 (2000).
11. Warner, J. R. The economics of ribosome biosynthesis in yeast. *Trends Biochem. Sci.* **24,** 437–440 (1999).
12. Zhou, Z. L. *et al.* The protein Aly links pre-messenger-RNA splicing to nuclear export in metazoans. *Nature* **407,** 401–405 (2000).
13. Huang, Y. & Steitz, J. A. Splicing factors SRp20 and 9G8 promote the nucleocytoplasmic export of mRNA. *Mol. Cell* **7,** 899–905 (2001).
14. Bruhn, L., Munnerlyn, A. & Grosschedl, R. ALY, a context-dependent coactivator of LEF-1 and AML-1, is required for TCRα enhancer function. *Genes Dev.* **11,** 640–653 (1997).
15. Virbasius, C. M., Wagner, S. & Green, M. R. A human nuclear-localized chaperone that regulates dimerization, DNA binding, and transcriptional activity of bZIP proteins. *Mol. Cell* **4,** 219–228 (1999).
16. Hellmuth, K. *et al.* Yeast Los1p has properties of an exportin-like nucleocytoplasmic transport factor for tRNA. *Mol. Cell. Biol.* **18,** 6364–6386 (1998).
17. Siniossoglou, S. *et al.* A novel complex of nucleoporins, which includes Sec13p and a Sec13p homolog, is essential for normal nuclear pores. *Cell* **84,** 265–275 (1996).
18. Luo, M.-J. *et al.* Pre-mRNA splicing and mRNA export linked by direct interactions between UAP56 and Aly. *Nature* (this issue).

Supplementary information is available on *Nature*'s World-Wide Web site (http://www.nature.com) or as paper copy from the London editorial office of *Nature*.

Acknowledgements

We are grateful to R. Grosschedl for GST–Aly, J. Braspenning for L20GST-NPL3, J. Beggs for *prp4-1* and *prp16-2* mutants, and D. Tollervey for the strain *GAL10::ProtA-RRP41* (P118). We thank R. Reed and the members of the Reed lab for critical reading of the manuscript. E.H. was a recipient of grants from the Deutsche Forschungsgemeinschaft and Fonds der Chemischen Industrie.

Correspondence and requests for materials should be addressed to E.H. (e-mail: cg5@ix.urz.uni-heidelberg.de).

corrections

A mouse knock-in model exposes sequential proteolytic pathways that regulate p27^{Kip1} in G1 and S phase

Nisar P. Malek, Holly Sundberg, Seth McGrew, Keiko Nakayama, Themis R. Kyriakides & James M. Roberts

Nature **413,** 323–327 (2001).

In this Letter, the last name of Themis R. Kyriakides was misspelled as 'Kyriakidis'. □

CREB regulates hepatic gluconeogenesis through the coactivator PGC-1

Stephan Herzig, Fanxin Long, Ulupi S. Jhala, Susan Hedrick, Rebecca Quinn, Anton Bauer, Dorothea Rudolph, Gunther Schutz, Cliff Yoon‖, Pere Puigserver, Bruce Spiegelman & Marc Montminy

Nature **413,** 179–183 (2001).

In the third sentence, "hyperglycaemia" should have read "hypoglycaemia". The corrected sentence is: "Here we show that mice carrying a targeted disruption of the cyclic AMP (cAMP) response element binding (CREB) protein gene, or overexpressing a dominant-negative CREB inhibitor, exhibit fasting hypoglycaemia and reduced expression of gluconeogenic enzymes." □

erratum

A titanosilicate molecular sieve with adjustable pores for size-selective adsorption of molecules

Steven M. Kuznicki, Valerie A. Bell, Sankar Nair, Hugh W. Hillhouse, Richard M. Jacubinas, Carola M. Braunbarth, Brian H. Toby & Michael Tsapatsis

Nature **412,** 720–724 (2001).

Correspondence and requests for materials relating to the structural analysis in this Letter should be addressed to Michael Tsapatsis (e-mail: tsapatsi@ecs.umass.edu). □

A mouse knock-in model exposes sequential proteolytic pathways that regulate p27^{Kip1} in G1 and S phase

Nisar P. Malek*†‡, Holly Sundberg†‡, Seth McGrew*†, Keiko Nakayama§, Themis R. Kyriakidis‖ & James M. Roberts*†‖

** Howard Hughes Medical Institute and † Department of Basic Sciences, Fred Hutchinson Cancer Research Center, Seattle, Washington 98104, USA*
§ Laboratory of Embryonic and Genetic Engineering, Medical Institute of Bioregulation, Kyushu University, Fukuoka 812-8582, Japan
‖ Department of Biochemistry, University of Washington, Seattle, Washington 98104, USA

The protein p27^{Kip1} is an inhibitor of cell division[1]. An increase in p27 causes proliferating cells to exit from the cell cycle, and a decrease in p27 is necessary for quiescent cells to resume division[2,3]. Abnormally low amounts of p27 are associated with pathological states of excessive cell proliferation, especially cancers[4–8]. In normal and tumour cells, p27 is regulated primarily at the level of translation[9–11] and protein turnover. Phosphorylation of p27 on threonine 187 (T187) by cyclin-dependent kinase 2 (Cdk2) is thought to initiate the major pathway for p27 proteolysis[12–15]. To critically test the importance of this pathway *in vivo*, we replaced the murine p27 gene with one that encoded alanine instead of threonine at position 187 (p27^{T187A}). Here we show that cells expressing p27^{T187A} were unable to downregulate p27 during the S and G2 phases of the cell cycle, but that this had a surprisingly modest effect on cell proliferation both *in vitro* and *in vivo*. Our efforts to explain this unexpected result led to the discovery of a second proteolytic pathway for controlling p27, one that is activated by mitogens and degrades p27 exclusively during G1.

Phosphorylation of p27 on T187 by Cdk2 creates a binding site for a Skp2-containing E3 ubiquitin-protein ligase known as SCF[16–18]; ubiquitination of p27 by SCF results in degradation of p27 by the proteasome[19–22]. We tested the role of T187 phosphorylation in determining abundance of p27 protein and in controlling cell proliferation, by constructing a mouse strain that expresses a non-phosphorylatable form of p27 (p27^{T187A}) instead of the wild-type p27 protein. Control experiments showed that p27^{T187A} and wild-type p27 were equally able to inhibit cyclin E–Cdk2 when either histone 1 (H1) or the retinoblastoma (Rb) protein was used as a substrate *in vitro*[12]. Therefore, we attributed the effects of this mutation, as described below, to altered p27 regulation rather than to an intrinsic change in its molecular properties as a Cdk inhibitor. In brief, the *p27* gene was precisely replaced with an allele in which the codon for T187 was changed to one encoding A187. Previous experiments using cultured fibroblasts had shown that ectopic overexpression of p27^{T187A} imposed an irreversible G1 arrest[12]. Therefore, a '*lox-STOP-lox*' element was placed within the p27^{T187A} promoter so that the mutant allele could be conditionally activated with Cre recombinase (see Methods) (Fig. 1a). Mice heterozygous for *p27^{T187A}(lox-STOP-lox)* (see Methods) were bred to mice that constitutively express Cre recombinase in the germ line, which resulted in deletion of the *lox-STOP-lox* element. The *p27^{T187A}(Δlox-STOP-lox)* allele was bred to homozygosity and shown to express the p27^{T187A} protein at levels equivalent to the wild-type allele in all tissues (data not shown). Surprisingly, expression of p27^{T187A} did not affect viability or fertility. Consequently, all further experiments were performed on mice homozygous for the *p27^{T187A}(Δlox-STOP-lox)* allele and that did not contain the Cre recombinase transgene.

The effect of the T187A mutation on regulation of the p27 protein was determined by comparing the protein levels of p27 and p27^{T187A} in mouse embryonic fibroblasts (MEFs). The MEFs were made quiescent by serum deprivation and then stimulated to enter the cell cycle by re-addition of serum. In control MEFs, p27 protein declined to a low level 12–15 h after serum stimulation, a time that corresponded to the early/mid-G1 phase of the cell cycle, and it remained at a low level for the duration of the cell cycle (Fig. 1b). p27^{T187A} was expressed at the same level as wild-type p27 in quiescent MEFs, a result consistent with our observation that p27 and p27^{T187A} were expressed at equal levels in mouse tissues, which are composed largely of non-dividing cells. Serum stimulation caused the level of the p27^{T187A} protein to decline with kinetics similar to wild-type p27. This was consistent with the fact that decreased expression of p27 in serum-stimulated fibroblasts preceded activation of cyclin E–Cdk2 (ref. 9 and see also Supplementary Information Fig. 1). In contrast to the wild-type protein, however, p27^{T187A} re-accumulated as cells completed G1 and entered S phase. Indeed, in late S/G2 the amount of p27^{T187A} rose to a level that was similar to its abundance in quiescent cells. This was associated with an increased amount of p27 bound to cyclin A

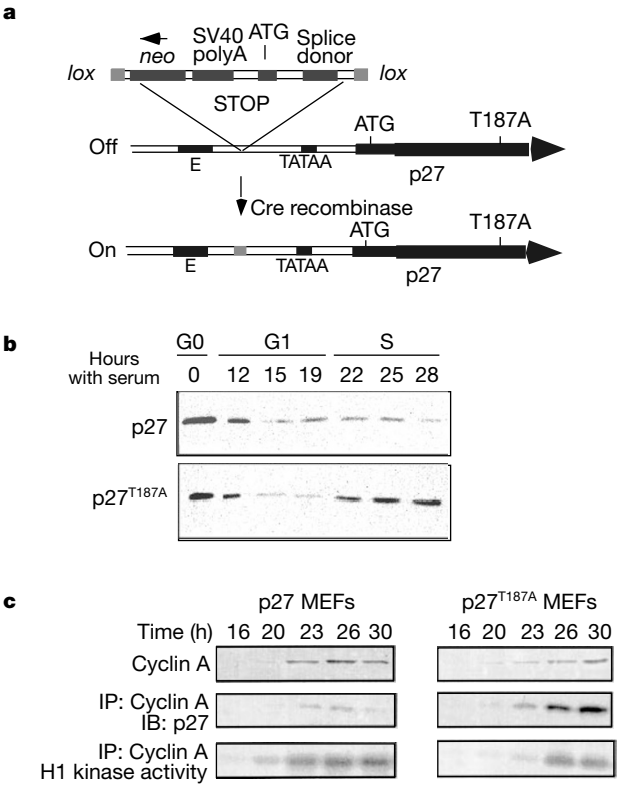

Figure 1 Replacement of the p27 gene with one encoding p27^{T187A}. **a**, Schematic diagram of the murine p27 gene modified to inducibly express a mutated p27 protein, p27^{T187A}. **b**, Immunoblot of wild-type p27 (top) and p27^{T187A} protein in serum-starved and re-stimulated MEFs. Analysis was performed using five independently isolated MEF strains from three different founder mice, and a representative result is shown. Cell cycle position at each point was determined by flow cytometry of nuclear DNA content, and by incorporation of BrdU into chromosomal DNA. **c**, MEFs expressing wild-type p27 or p27^{T187A} were arrested in G0 by serum starvation. Re-addition of serum caused synchronous re-entry into the cell cycle. Expression of cyclin A, cyclin A-associated p27, and cyclin A-associated H1 kinase activity were measured at each point. IB, western immunoblot; IP, immunoprecipitate.

‡ Present address: Department of Gastroenterology and Hepatology, and Institute for Molecular Biology, Hannover Medical School, Hannover 30625, Germany.

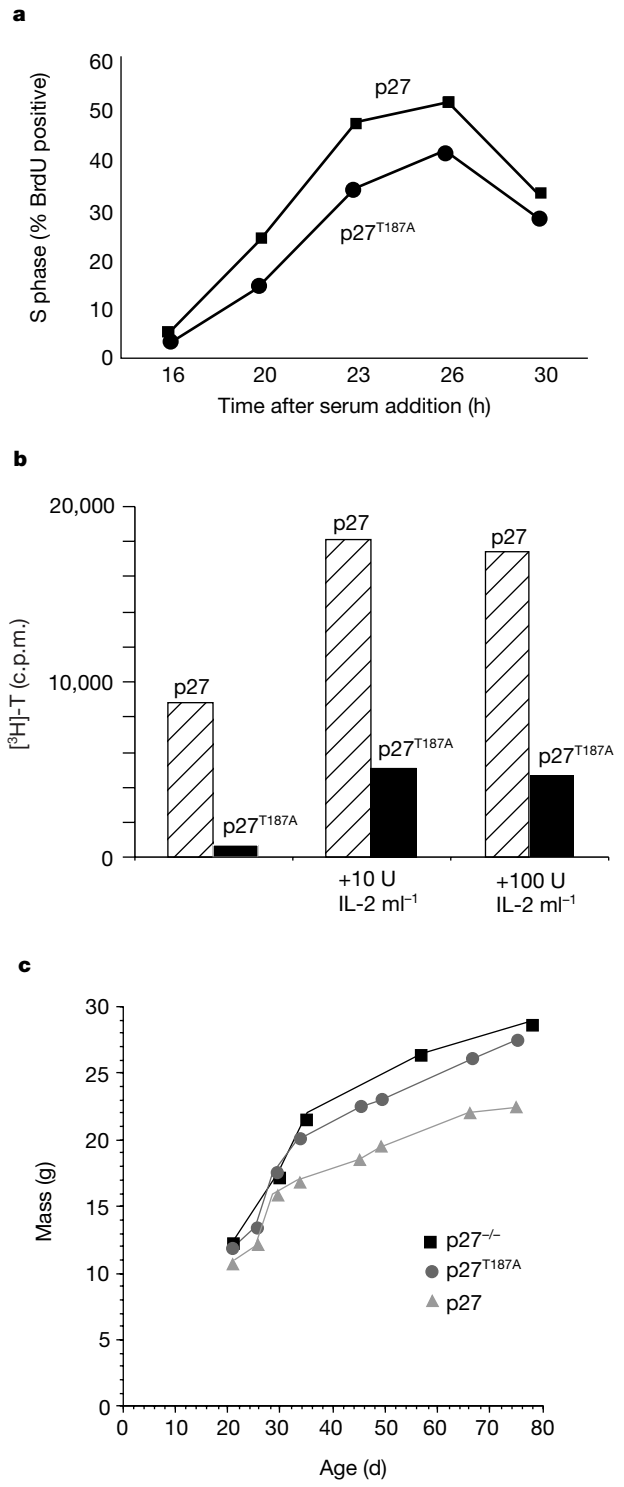

Figure 2 Effect of $p27^{T187A}$ on cell proliferation. **a**, Quiescent MEFs were stimulated to proliferate by re-feeding with serum. Percentage of cells in S phase was determined by pulse labelling with BrdU. The analysis was repeated using three independently isolated MEF strains from three different founder mice. A representative result is shown. **b**, Purified $CD4^+$ splenic T lymphocytes expressing either p27 or $p27^{T187A}$ were stimulated to proliferate with antibodies against the T-cell antigen receptor alone, or with anti-receptor antibodies plus the indicated amount of recombinant IL-2. Proliferation was measured by incorporation of $[^3H]$-thymidine ($[^3H]$-T) into DNA. All measurements were done in triplicate, using lymphocytes isolated from two different founder mice. **c**, Growth curves of female wild-type p27, p27-null and homozygous $p27^{T187A}$ mice. Each point represents an average of 30 mice. The p27 and $p27^{T187A}$ mice were littermates (F_2 hybrids, B6/C57 × 129/Sv). Mass data for the p27-null mice were obtained from an earlier study, which used mice of the same genetic background as those used here[2].

and a 50% reduction in cyclin A-associated kinase activity (Fig. 1c). There was no change in total levels of cyclin A protein, and the length of S phase was not altered. These experiments demonstrated that p27 was downregulated in a T187-dependent manner in S and G2, and independently of T187 (and Cdk2) in G1.

The absence of the T187-dependent pathway for p27 turnover had significant effects on cell proliferation in various cells and tissues of the $p27^{T187A}$ mutant mouse. In general we found that the rising levels of $p27^{T187A}$ that occurred in late G1/S/G2 cells created a barrier to cell cycle progression. However, the severity of the ensuing proliferation defect varied among cell types. A modest effect was seen in MEFs, where expression of $p27^{T187A}$ caused a 20–30% reduction in the number of cells that entered S phase after serum stimulation (Fig. 2a). A relatively greater defect was seen when purified splenic T lymphocytes that carry the CD4 antigen were stimulated to proliferate with antibodies directed against the T-cell antigen receptor. DNA replication was reduced by 80% in cells expressing $p27^{T187A}$ compared with control T cells (Fig. 2b). Addition of exogenous interleukin-2 (IL-2) partially restored proliferation of the cells expressing $p27^{T187A}$, suggesting that high levels of IL-2 might promote a T187-independent pathway for decreasing p27 levels.

A defect in cell proliferation was also observed in dermal keratinocytes expressing $p27^{T187A}$. Keratinocyte proliferation was induced *in vivo* by creating circular (4 mm diameter) punch wounds of full thickness (extending through the epidermis and dermis) in the skin overlying the scapula. The rate of healing was monitored by gross inspection and by histological examination at 4.5 days after wounding. Wound closure by regrowth of epithelial cells was delayed in the $p27^{T187A}$ mice. The epithelial gap (measured as the distance between the keratinocyte edges growing into the wound bed) made up 60 ± 5% of the entire wound in the $p27^{T187A}$ mice as compared with 35 ± 9% in the control mice ($n = 12$) (see Supplementary Information Fig. 2). This difference was most probably a result of an impaired proliferative response, as $p27^{T187A}$ keratinocytes at the wound edge displayed reduced incorporation of bromodeoxyuridine (BrdU) ($p27^{T187A}$ 13.5 ± 8.5% versus control 35 ± 5%). No difference was observed between $p27^{T187A}$ and control mice in the healing of incision wounds, which occurs mostly by epithelial cell migration rather than by proliferation (data not shown).

It was remarkable that, despite the restraint on cell proliferation created by the $p27^{T187A}$ mutation, mice expressing this protein developed normally and attained an average size that was even larger than wild-type mice (Fig. 2c). The mechanism underlying this is unknown, but it was important to rule out the possibility that the larger size of the mutant mice was due to increased cell proliferation, because this would be inconsistent with the proliferative impairment of $p27^{T187A}$-expressing cells, as described above. To address this issue we examined cell proliferation in the thymus of the $p27^{T187A}$ mice, which, like all other organs, was enlarged in proportion to overall body size. In contrast to what is observed in p27-knockout mice[5], thymocytes expressing $p27^{T187A}$ did not show an increased amount of cell proliferation as determined by BrdU labelling (data not shown). This indicates that the T187A mutation and the *p27* gene deletion affected organ size by different mechanisms. Other phenotypes associated with p27 deficiency were also absent in the mice expressing $p27^{T187A}$, including female sterility, pituitary tumorigenesis and disrupted retinal architecture. Hence, there is no evidence that the $p27^{T187A}$ mutation results in a hypoactive allele. We are investigating the effect of the $p27^{T187A}$ mutation on apoptosis and cell size to determine whether these might contribute to increased growth rates and increased body size. However, staining kidneys, spleens and livers from 2-month-old mice with TUNEL (TdT-mediated dUTP nick end labelling) did not reveal any differences between control mice and mice expressing $p27^{T187A}$, and flow cytometric measurements did not show increased

size of $p27^{T187A}$ thymocytes from 8-week-old mice (see Supplementary Information Fig. 3).

The above experiments showed that p27 abundance is controlled by two mechanisms, the first acting in early/mid-G1 cells and the second in late G1, S and G2. We made the unexpected observation that increased turnover of the p27 protein contributed not only to the T187 pathway for p27 regulation, but to the earlier G1 pathway as well (Fig. 3a). In quiescent cells, p27 was relatively stable, with a half-life of 10–12 h. Serum stimulation decreased p27 stability, reducing its half-life to about 2 h in both G1- and S-phase cells. $p27^{T187A}$ was also stable in quiescent cells, and after serum stimulation became unstable in mid-G1 similarly to the wild-type protein. An independent method for measuring protein half-lives (pulse-chase) confirmed that wild-type p27 and $p27^{T187A}$ had equally short half-lives (<4 h) in G1-phase MEFs. In S-phase cells, however, $p27^{T187A}$ was stable, acquiring a long half-life very similar to that in quiescent, mitogen-starved cells. Thus, rapid turnover of p27 in S-phase cells requires T187, whereas the rapid turnover of p27 in G1 cells does not. These data also implied that the proteolytic pathway that degraded p27 in G1 cells was not operative in S phase.

This G1-specific turnover pathway for p27 is not a unique feature of cells as they exit quiescence, but rather occurs during each mitotic cycle. Quiescent MEFs were stimulated with serum mitogens for 18 h, at which time they were separated by flow cytometry into G1- and S-phase populations. Levels of the p27 protein were lower in G1 cells than in quiescent cells. In the S-phase population, however, the abundance of wild-type p27 declined further, whereas the opposite occurred in MEFs expressing $p27^{T187A}$ (Fig. 3b). The S-phase cells were then replated and allowed to progress through the division cycle until a time when 80% of the cells had entered the next G1 phase. The abundance of $p27^{T187A}$ declined again in the second G1, just as it had in the first G1, demonstrating the periodic nature of the G1-turnover pathway.

The turnover of p27 in G1 cells was proteasome dependent. Quiescent, serum-starved MEFs were re-stimulated with serum and 6 h later treated with MG132, an inhibitor of proteasomal proteolysis. This prevented the normal decrease in p27 protein levels that occurs in mid-G1 (Fig. 3c).

Phosphorylation of p27 on T187 triggers its ubiquitination by the Skp2-containing SCF E3 complex, and its subsequent turnover in the proteasome[12–14,19–22]. This pathway is operational in S- and G2-phase cells, after Cdk2 is activated by cyclins E and A. Surprisingly, we found that the G1-specific turnover of p27 was also mediated by Skp2 in MEFs, but independently of phosphorylation on T187. Extracts from asynchronously proliferating MEFs (not shown) and MEFs synchronized in G1 (Fig. 4a) were immunoprecipitated with anti-Skp2 antibodies. p27 and $p27^{T187A}$ were detected in equal abundance in Skp2 complexes. The binding of Skp2 to both p27 and $p27^{T187A}$ was phosphorylation dependent, because treatment of isolated p27–Skp2 and $p27^{T187A}$–Skp2 complexes with a protein phosphatase disrupted the interaction (Fig. 4b, Supplementary Information Fig. 4). The phosphorylation site(s) on p27 and/or Skp2 that mediate this interaction have not yet been identified. We further showed that Skp2 was essential for the turnover of p27 in G1 cells, because levels of p27 protein did not decline, either in G1 or in S phase, in serum-stimulated, early-passage, Skp2-null MEFs (Fig. 4c)[23]. In conclusion, in MEFs the trigger for p27 turnover differs in G1 and S phase, but both pathways ultimately lead to the degradation of p27 by Skp2 and proteasome-dependent mechanisms.

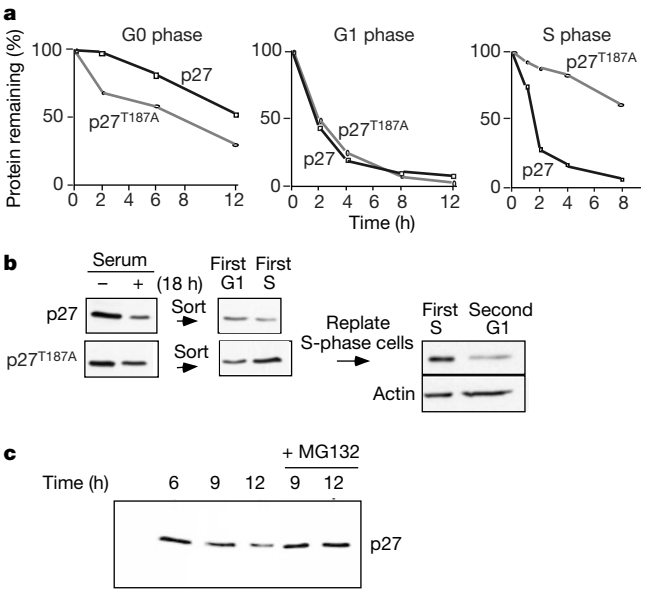

Figure 3 Cell-cycle-dependent proteolysis of p27. **a**, The half-lives of p27 and $p27^{T187A}$ were measured in G0-, G1- and S-phase MEFs. Cells were synchronized by serum starvation (G0) and re-feeding (G1 is 12 h after re-feeding; S is 24 h after re-feeding). **b**, Levels of p27 protein were determined by immunoblotting of cell extracts from cells synchronized through two cell cycles. See text for details. **c**, Control ($p27^{+/+}$) MEFs were synchronized by serum starvation and then stimulated to enter the cell cycle by re-feeding with serum. One group of cells was allowed to proceed through G1, while the other group was treated with the proteasome inhibitor MG132 (10 μM) at 6 h after serum stimulation. Levels of p27 protein were then measured by immunoblotting at the indicated time points.

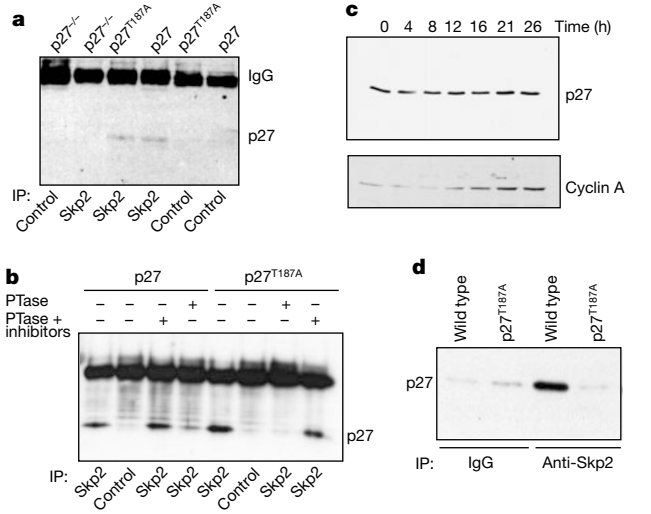

Figure 4 Turnover of p27 in G1- and in S-phase MEFs requires Skp2. **a**, Skp2 was immunoprecipitated from MEFs synchronized in G1 by serum starvation and re-feeding. The presence of associated p27 (or $p27^{T187A}$) was determined by immunoblotting. Control immunoprecipitations used an irrelevant immunoglobulin-γ (IgG, anti-cytochrome C), and a control immunoprecipitation from p27-null MEFs is also shown. **b**, A plasmid encoding Skp2 was cotransfected into human 293T cells together with a plasmid encoding either p27 or $p27^{T187A}$. Whole-cell extracts were immunoprecipitated with anti-Skp2 or control (anti-cytochrome C) antibodies and, as indicated, immunoblotted directly for associated p27, treated with alkaline phosphatase (PTase) before immunoblotting, or treated with alkaline phosphatase plus phosphatase inhibitors. **c**, Quiescent $Skp2^{-/-}$ MEFs were stimulated to re-enter the cell cycle by addition of serum, and levels of p27 protein were determined at the indicated time points by immunoblotting. $Skp2^{-/-}$ MEFs progressed through G1 and entered S phase about 16 h after serum stimulation, as determined by the timing of cyclin A expression. **d**, The binding of p27 and $p27^{T187A}$ to Skp2 was determined in extracts of purified thymocytes from control and homozygous $p27^{T187A}$ mice. IP, immunoprecipitate.

In contrast to the situation in MEFs, a $p27^{T187A}$–Skp2 complex was not detected in purified murine thymocytes (Fig. 4d). This reflected the relatively more severe effect of the $p27^{T187A}$ mutation on proliferation in these cells than in MEFs, and underscored the importance of a T187-independent pathway for p27 turnover in allowing for normal cell proliferation. However, it is not yet known whether the enhanced proliferation of $p27^{T187A}$ thymocytes caused by exogenous IL-2 (Fig. 2b) is due to stimulation of the $p27^{T187A}$–Skp2 interaction or whether it may be through a Skp2-independent mechanism for p27 turnover.

Our data show that T187-dependent turnover of p27 is important for normal regulation of p27 and normal control of cell division. However, contrary to what might have been expected, inactivating this pathway has neither a universal nor a severe effect on cell proliferation. This may be explained, at least in part, by a previously unrecognized T187-independent pathway for p27 degradation that is activated during each G1 phase of the cell cycle. This pathway allows many cells expressing $p27^{T187A}$ to complete the cell cycle before the re-accumulation of p27 in S phase can stop it. The T187 pathway, which keeps p27 levels low for the duration of S and G2, may allow the cell to slow its progress through this part of the cell cycle (for instance, in response to DNA damage) without experiencing continually rising and ultimately inhibitory amounts of p27.

Our major conclusion is that two proteolytic pathways act in sequence during the cell cycle to control p27 abundance. The first pathway functions during early–mid G1 and is triggered by mitogens. It may be activated by Ras and Myc, and underlie the ability of these proteins to reduce p27 abundance independently of serum stimulation[24,25] and independently of Cdk2 (ref. 24). Inhibition of p27 at the level of translation[9–11] and by sequestration into cyclin D–Cdk complexes[26] also contribute to downregulation of p27 during the early–mid-G1 cell cycle period. Downregulation of p27 by the concerted action of these pathways results in the initial production of active cyclin E–Cdk2, and consequently the onset of the second pathway for p27 turnover. This second pathway operates in late G1, S and G2, and is dependent on Cdk2-mediated phosphorylation of p27 on T187. Once initiated, this second pathway would be amplified by a positive-feedback loop, and therefore would continue even if the initial mitogenic stimulus were withdrawn. In this way, inactivation of p27 switches in mid G1 from being mitogen dependent to being mitogen independent, which is analogous to the consecutive mitogen-dependent and mitogen-independent pathways that inactivate Rb during the same cell cycle interval[27]. Sequentially acting pathways that inactivate key cell cycle inhibitors may be the biochemical underpinnings of the cell cycle transition from mitogen dependence to mitogen independence, which has been called the G1 restriction point[28]. □

Methods

Mice

To construct the genomic targeting vector, a 5.9-kilobase (kb) *Bam*HI fragment was isolated from a previously described 17-kb *Not*I fragment that contains the entire coding region of the *p27* gene obtained from a mouse 129/Svl genomic library[2]. Threonine 187 of exon 2 was mutated to alanine (ACG→GCG) to create the $p27^{T187A}$ allele. A 3-kb *Sac*I fragment containing a *pgk*-driven neomycin-resistance gene and a transcription termination cassette isolated as a *Bam*HI–*Hin*dIII fragment from pBS302 (Gibco BRL) was flanked with *loxP* sequences and inserted into a *Sac*I site in the *p27* promoter, creating the construct $p27^{T187A}$*(5.9-Neo/STOP)*. The $p27^{T187A}$*(5.9-Neo/STOP)* construct was then cloned into the pPNT vector[2], thus creating the genomic targeting vector. The targeting vector was linearized with *Not*I and transduced by electroporation into mouse XY AK7 embryonic stem cells.

Embryonic stem cells were selected in 400 μg ml^{-1} G418 and 0.4 μM fialuridine. Colonies of embryonic stem cells were screened for homologous recombination events by Southern blotting using a probe external to the 5′ end of the targeting construct. In all five embryonic stem cell clones used for blastocyst injection, integration of the T187A mutation was verified by sequencing. $p27^{T187A}$ embryonic stem cells were introduced by microinjection into C57/B6J mouse embryos at 5 d after conception. Germline transmission was identified in male chimaeras representing three separate embryonic stem cell clones. To excise the *neo/STOP* cassette from the *p27* gene, chimaeric male mice were bred with female CMV-Cre transgenic mice (TgN(CMV-Cre)1AN)[29]. Excision of the *neo/STOP* cassette was verified by polymerase chain reaction (PCR) using primers derived from the $p27^{T187A}$ genomic sequence upstream of the *Sac*I site (Y1, GAGCAGGTTTGTTGGCAGTCGTACACCTCC), from the neomycin gene (A4, CGTGGGATCATTGTTTTTCTCTTG), and from the genomic sequence downstream of the *Sac*I site (H3, CCAATATGGCGGTGGAA GGGAGGCTGA). Homozygous integration of the T187A mutation was confirmed by the presence of a 34-base pair (bp) (*loxP* site) insertion into the wild-type 0.25-kb PCR fragment using primers Y1 and H3.

MEFs

Males and females heterozygous for $p27^{T187A}$ were crossed and embryos were dissected 12.5–13.5 d after detection of vaginal plugs. The head and internal organs were removed and the embryos were minced and incubated in 0.05% trypsin for 5 min. The cells were resuspended in DMEM supplemented with 10% FBS. After centrifugation the supernatant was discarded and the cell suspension from each embryo was cultivated on a 10-cm dish in 8 ml DMEM with 10% FBS until confluency was reached. After this time, the cells were treated with trypsin, counted and plated at 1.4×10^6 cells per 10-cm dish every 3 d.

Cell culture

In all experiments, unless otherwise noted, cell cycle position of synchronized cells was determined by flow cytometric measurement of nuclear DNA content. Passage 2–3 MEFs were plated at 1.4×10^6 per 10-cm dish grown in DMEM with 10% FBS for 3 d, after which the medium was removed, the plates washed with PBS and the cells incubated in DMEM containing 0.1% FBS for 72 h. The cells were then washed with PBS, treated with trypsin, counted and resuspended in DMEM containing 10% FBS at 1.4×10^6 cells per 10-cm dish and 0.5×10^5 cells per 6-cm dish. For each time point, the cells were labelled with 10 μM BrdU (Sigma) for 30 min, scraped off the plate, washed with PBS and fixed in 70% ethanol for at least 24 h. Nuclei were purified and labelled with 100 μl anti-BrdU-fluoroscein isothiocyanate (FITC) antibody (PharMingen). After this incubation, nuclei were treated with RNase A, counterstained with propidium iodide (100 μg ml^{-1}) and analysed on a Becton Dickinson flow cytometer using Becton Dickinson Cell Quest software.

To separate G1- from S-phase cells, cells were labelled with Hoechst Stain (Sigma) (10 μg ml^{-1}) for 30 min, treated with trypsin and separated according to DNA content on a Vantage SE flow cytometer (BD systems) using Cell Quest software. For p27 half-life measurements, cycloheximide (CHX, 10 μg ml^{-1} final concentration) was added to the cells at the indicated times. p27 protein levels were determined by immunoblotting. Cell cycle position was verified by flow cytometry and BrdU labelling. The resulting autoradiograms were scanned and the intensity of the p27 bands quantified using Image Quant software (Molecular Dynamics) and normalized to actin controls.

Isolation and stimulation of T lymphocytes

Splenic $CD4^+$ T cells were purified after red-cell lysis (Whole Blood Erythrocyte Lysing Kit, R&D Sytems). Mononuclear cells were enriched using Ficoll-gradient centrifugation. $CD4^+$ T cells were isolated using mouse T Cell CD4 Subset Columns (R&D Systems). $CD4^+$ T cells were activated with plate-bound anti-CD3 antibody with or without the addition of recombinant mouse IL-2 (PharMingen) using concentrations as indicated for the individual experiments. Seventy-two hours after stimulation, T cells were labelled with [^{3}H]-thymidine for 4 h, collected and the incorporation of radioactivity into DNA was determined.

Immunoblotting

The antibodies used in these experiments were mouse monoclonal anti-p27 (Transduction), rabbit polyclonal anti-cyclin A (Santa Cruz), anti-actin (Santa Cruz), anti-Skp2 (Santa Cruz) and anti-Cdk2 (Santa Cruz). For immunoprecipitation of p27–Skp2 complexes, early-passage MEFs were synchronized as described above, and cells were lysed in RIPA buffer. Cell extracts were pre-cleared in protein A sepharose (Repligen) for 1 h and incubated with anti-Skp2 antibodies (Zymed GP45 and Santa Cruz H-435) overnight. Control immunoprecipitations used anti-cytochrome C antibodies (Santa Cruz, H104). After incubation with protein A sepharose, the beads were washed with RIPA, boiled in SDS sample buffer and separated on a 12% polyacrylamide gel. p27 was detected using anti-p27 antibodies. For detection of p27–Skp2 complexes in thymocytes, thymuses were removed from 2–6-week-old mice, organs were homogenized using glass slides, cells lysed in RIPA and processed as described above. For phosphatase treatment of p27–Skp2 complexes, 293 cells were transfected with expression vectors (CS2 with Skp2, p27 and $p27^{T187A}$). Cells were lysed in RIPA and immunoprecipitated with anti-Skp2 antibodies (Santa Cruz). p27–Skp2 complexes bound to sepharose beads were treated with alkaline phosphatase buffer (15 ml) with or without 5 U alkaline phosphatase (30 min at 30 °C in 20 μl) (both Boehringer Manheim), or alkaline phosphatase plus a cocktail of phosphatase inhibitors (10 mM β-glycerophosphate, 100 μM sodium vanadate, 50 mM sodium fluoride). Beads were then washed three times with RIPA, boiled in SDS sample buffer, separated on a 12% polyacrylamide gel, and immunoblotted for p27.

Wound healing

Full-thickness punch wounds (4 mm diameter) were applied. Animals were injected with BrdU (1 mg ml^{-1}, 30 μl g^{-1}) 16 h before they were killed. Wounds were excised, fixed and embedded in paraffin 4.5 d after wounding[30]. Wounds were stained with anti-BrdU antibody (AB1, NeoMarkers); BrdU staining was visualized using the Darko Ark Kit and

counterstained with haematoxylin and eosin. Wound sizes and epithelial gap diameters were determined by optical micrometer measurements at ×100 magnification.

Received 25 May; accepted 18 July 2001.

1. Sherr, C. J. & Roberts, J. M. Inhibitors of mammalian G1 cyclin-dependent kinases. *Genes Dev.* **9,** 1149–1163 (1995).
2. Fero, M. L. *et al.* A syndrome of multiorgan hyperplasia with features of gigantism, tumorigenesis, and female sterility in p27(Kip1)-deficient mice. *Cell* **85,** 733–744 (1996).
3. Coats, S. *et al.* A new pathway for mitogen-dependent cdk2 regulation uncovered in p27(Kip1)-deficient cells. *Curr. Biol.* **9,** 163–173 (1999).
4. Ophascharoensuk, V., Fero, M. L., Hughes, J., Roberts, J. M. & Shankland, S. J. The cyclin-dependent kinase inhibitor p27Kip1 safeguards against inflammatory injury. *Nature Med.* **4,** 575–580 (1998).
5. Fero, M. L., Randel, E., Gurley, K. E., Roberts, J. M. & Kemp, C. J. The murine gene $p27^{Kip1}$ is haplo-insufficient for tumour suppression. *Nature* **396,** 177–180 (1998).
6. Porter, P. L. *et al.* Expression of cell-cycle regulators $p27^{Kip1}$ and cyclin E, alone and in combination, correlate with survival in young breast cancer patients. *Nature Med.* **3,** 222–225 (1997).
7. Tan, P. *et al.* The cell cycle inhibitor p27 is an independent prognostic marker in small (T1a,b) invasive breast carcinomas. *Cancer Res.* **57,** 1259–1263 (1997).
8. Catzavelos, C. *et al.* Decreased levels of the cell-cycle inhibitor $p27^{Kip1}$ protein: prognostic implications in primary breast cancer. *Nature Med.* **3,** 227–230 (1997).
9. Agrawal, D. *et al.* Repression of $p27^{kip1}$ synthesis by platelet-derived growth factor in BALB/c 3T3 cells. *Mol. Cell. Biol.* **16,** 4327–4336 (1996).
10. Hengst, L. & Reed, S. I. Translational control of $p27^{Kip1}$ accumulation during the cell cycle. *Science* **271,** 1861–1864 (1996).
11. Millard, S. S., Vidal, A., Markus, M. & Koff, A. A U-rich element in the 5′ untranslated region is necessary for the translation of p27 mRNA. *Mol. Cell. Biol.* **20,** 5947–5959 (2000).
12. Sheaff, R. J., Groudine, M., Gordon, M., Roberts, J. M. & Clurman, B. E. Cyclin E-CDK2 is a regulator of $p27^{Kip1}$. *Genes Dev.* **11,** 1464–1478 (1997).
13. Vlach, J., Hennecke, S., Alevizopoulos, K., Conti, D. & Amati, B. Growth arrest by the cyclin-dependent kinase inhibitor $p27^{Kip1}$ is abrogated by c-Myc. *EMBO J.* **15,** 6595–6604 (1996).
14. Muller, D. *et al.* Cdk2-dependent phosphorylation of p27 facilitates its Myc-induced release from cyclin E/cdk2 complexes. *Oncogene* **15,** 2561–2576 (1997).
15. Pagano, M. *et al.* Role of the ubiquitin–proteasome pathway in regulating abundance of the cyclin-dependent kinase inhibitor p27. *Science* **269,** 682–685 (1995).
16. Feldman, R. M., Correll, C. C., Kaplan, K. B. & Deshaies, R. J. A complex of Cdc4p, Skp1p, and Cdc53p/cullin catalyzes ubiquitination of the phosphorylated CDK inhibitor Sic1p. *Cell* **91,** 221–230 (1997).
17. Bai, C. *et al.* SKP1 connects cell cycle regulators to the ubiquitin proteolysis machinery through a novel motif, the F-box. *Cell* **86,** 263–274 (1996).
18. Skowyra, D., Craig, K. L., Tyers, M., Elledge, S. J. & Harper, J. W. F-box proteins are receptors that recruit phosphorylated substrates to the SCF ubiquitin-ligase complex. *Cell* **91,** 209–219 (1997).
19. Sutterluty, H. *et al.* $p45^{SKP2}$ promotes $p27^{Kip1}$ degradation and induces S phase in quiescent cells. *Nature Cell Biol.* **1,** 207–214 (1999).
20. Rolfe, M., Chiu, M. I. & Pagano, M. The ubiquitin-mediated proteolytic pathway as a therapeutic area. *J. Mol. Med.* **75,** 5–17 (1997).
21. Carrano, A. C., Eytan, E., Hershko, A. & Pagano, M. SKP2 is required for ubiquitin-mediated degradation of the CDK inhibitor p27. *Nature Cell Biol.* **1,** 193–199 (1999).
22. Tsvetkov, L. M., Yeh, K. H., Lee, S. J., Sun, H. & Zhang, H. p27(Kip1) ubiquitination and degradation is regulated by the SCF(Skp2) complex through phosphorylated Thr187 in p27. *Curr. Biol.* **9,** 661–664 (1999).
23. Nakayama, K. *et al.* Targeted disruption of Skp2 results in accumulation of cyclin E and p27(Kip1), polyploidy and centrosome overduplication. *EMBO J.* **19,** 2069–2081 (2000).
24. Leone, G., DeGregori, J., Sears, R., Jakoi, L. & Nevins, J. R. Myc and Ras collaborate in inducing accumulation of active cyclin E/Cdk2 and E2F. *Nature* **387,** 422–426 (1997).
25. O'Hagan, R. C. *et al.* Myc-enhanced expression of Cul1 promotes ubiquitin-dependent proteolysis and cell cycle progression. *Genes Dev.* **14,** 2185–2191 (2000).
26. Sherr, C. J. & Roberts, J. M. CDK inhibitors: positive and negative regulators of G1-phase progression. *Genes Dev.* **13,** 1501–1512 (1999).
27. Hatakeyama, M. *et al.* The cancer cell and the cell cycle clock. *Cold Spring Harb. Symp. Quant. Biol.* **59,** 1–10 (1994).
28. Pardee, A. B. A restriction point for control of normal animal cell proliferation. *Proc. Natl Acad. Sci. USA* **71,** 1286–1290 (1974).
29. Nagy, A. *et al.* Dissecting the role of N-myc in development using a single targeting vector to generate a series of alleles. *Curr. Biol.* **8,** 661–664 (1998).
30. Kyriakides, T. R., Tam, J. W. & Bornstein, P. Accelerated wound healing in mice with a disruption of the thrombospondin 2 gene. *J. Invest. Dermatol.* **113,** 782–787 (1999).

Supplementary information is available on *Nature*'s World-Wide Web site (http://www.nature.com) or as paper copy from the London editorial office of *Nature*.

Acknowledgements

We thank B. Clurman, R. Sheaff, K.-I. Nakayama, B. Carter, M. Groudine, B. Luscher and members of the Roberts laboratory for advice, suggestions and reagents. M. Black and N. Jiang provided expert technical assistance with flow cytometry and with the generation of mutant mouse strains. We thank P. Porter for help with TUNEL staining. N.P.M. was supported by a grant from the Deutche Forschungsgemeinschaft. T.R.K. was supported by The National Science Foundation through the University of Washington Engineered Biomaterials Engineering Research Center. H.S. was supported by a grant from the National Institutes of Health. This work was supported by a grant from the National Institutes of Health to J.M.R. and by a George M. O'Brien Kidney Research Center award. J.M.R. is an Investigator of the Howard Hughes Medical Institute.

Correspondence and requests for materials should be addressed to J.M.R. (e-mail: jroberts@fred.fhcrc.org).

RNA-binding protein Nrd1 directs poly(A)-independent 3′-end formation of RNA polymerase II transcripts

Eric J. Steinmetz*†, Nicholas K. Conrad†‡, David A. Brow* & Jeffry L. Corden‡

* *Department of Biomolecular Chemistry, University of Wisconsin Medical School, Madison, Wisconsin 53706-1532, USA*
‡ *Department of Molecular Biology and Genetics, The Johns Hopkins University School of Medicine, Baltimore, Maryland 21205, USA*
† *These authors contributed equally to this work*

A eukaryotic chromosome contains many genes, each transcribed separately by RNA polymerase (pol) I, II or III. Transcription termination between genes prevents the formation of polycistronic RNAs and anti-sense RNAs, which are generally detrimental to the correct expression of genes. Terminating the transcription of protein-coding genes by pol II requires a group of proteins that also direct cleavage and polyadenylation of the messenger RNA in response to a specific sequence element, and are associated with the carboxyl-terminal domain of the largest subunit of pol II (refs 1–6). By contrast, the *cis*-acting elements and *trans*-acting factors that direct termination of non-polyadenylated transcripts made by pol II, including small nucleolar and small nuclear RNAs, are not known. Here we show that read-through transcription from yeast small nucleolar RNA and small nuclear RNA genes into adjacent genes is prevented by a *cis*-acting element that is recognized, in part, by the essential RNA-binding protein Nrd1. The RNA-binding protein Nab3, the putative RNA helicase Sen1, and the intact C-terminal domain of pol II are also required for efficient response to the element. The same proteins are required for maintaining normal levels of Nrd1 mRNA, indicating that these proteins may control elongation of a subset of mRNA transcripts.

We previously identified yeast Nrd1 as an essential nuclear RNA-binding protein that directs 3′ truncation of reporter gene mRNA transcripts in response to an artificial element containing a Nrd1-binding sequence[7,8]. Nrd1-dependent 3′ truncation also requires Sen1, an essential nuclear helicase-like protein that has been implicated in biogenesis of particular small nucleolar (sno) RNAs[9–11]. The properties of Nrd1 suggested that it might direct termination by pol II, although it is not a known component of the well-characterized pre-mRNA cleavage and polyadenylation apparatus.

Direct evidence that snoRNAs might be natural targets for Nrd1 was first obtained from expression profiling of poly(A)$^+$ RNA derived from temperature-sensitive *nrd1* yeast strains as compared with wild type (see Methods). Several open reading frames (ORFs) exhibiting increased expression in the *nrd1* mutant strain are located downstream of snoRNA genes in the yeast genome. For example, increased expression of transcripts containing the *TRS31* coding region, which is located immediately downstream of the gene encoding snR13 snoRNA (Fig. 1a), is observed in *nrd1* mutant strains.

Northern blot analysis of snR13 and Trs31 transcripts from wild-type and *nrd1* mutant strains shows the accumulation in the mutant strain of a new RNA species, which is larger than the normal Trs31 mRNA, that is detected by probes complementary to either mature snR13 RNA or Trs31 mRNA (Fig. 1b). The abundance of this extended product increases rapidly and markedly when the *nrd1* mutant is shifted from permissive to restrictive temperature. The 5′ end of this product coincides with the snR13 RNA 5′ end, as shown

Immunofluorescence

CHP100 cells or transfected BHK cells were plated on glass coverslips (Baxter) and stimulated with 5–10 $\mu g\,ml^{-1}$ pre-clustered EphB2-Fc for the desired time points. Cells were fixed and then processed according to standard procedures. Images were acquired with a confocal microscope (Leica DM DRB or Zeiss LSM 510) and processed with Adobe Photoshop. See supplementary Information for detailed methods.

Received 22 May; accepted 17 July 2001.

1. Henkemeyer, M. *et al.* Nuk controls pathfinding of commissural axons in the mammalian central nervous system. *Cell* **86,** 35–46 (1996).
2. Birgbauer, E., Cowan, C. A., Sretavan, D. W. & Henkemeyer, M. Kinase independent function of EphB receptors in retinal axon pathfinding to the optic disc from dorsal but not ventral retina. *Development* **127,** 1231–1241 (2000).
3. Mellitzer, G., Xu, Q. & Wilkinson, D. G. Eph receptors and ephrins restrict cell intermingling and communication. *Nature* **400,** 77–81 (1999).
4. Xu, Q., Mellitzer, G., Robinson, V. & Wilkinson, D. G. *In vivo* cell sorting in complementary segmental domains mediated by Eph receptors and ephrins. *Nature* **399,** 267–271 (1999).
5. Holland, S. J. *et al.* Bidirectional signaling through the Eph family receptor Nuk and its transmembrane ligands. *Nature* **383,** 722–725 (1996).
6. Bruckner, K., Pasquale, E. B. & Klein, R. Tyrosine phosphorylation of transmembrane ligands for Eph receptors. *Science* **275,** 1640–1643 (1997).
7. George, S. E. *et al.* The VAB-1 Eph receptor tyrosine kinase functions in neural and epithelial morphogenesis in *C. elegans*. *Cell* **92,** 633–643 (1998).
8. Davy, A. *et al.* Compartmentalized signaling by GPI-anchored ephrin-A5 requires the Fyn tyrosine kinase to regulate cellular adhesion. *Genes Dev.* **13,** 3125–3135 (1999).
9. Margolis, B. *et al.* High-efficiency expression/cloning of epidermal growth factor-receptor-binding proteins with Src homology 2 domains. *Proc. Natl Acad. Sci. USA* **89,** 8894–8898 (1992).
10. Chen, M. *et al.* Identification of Nck family genes, chromosomal localization, expression, and signaling specificity. *J. Biol. Chem.* **273,** 25171–25178 (1998).
11. Tu, Y., Li, F. & Wu, C. Nck-2, a novel Src homology2/3-containing adaptor protein that interacts with the LIM-only protein PINCH and components of growth factor receptor kinase-signaling pathways. *Mol. Biol. Cell* **9,** 3367–3382 (1998).
12. Garrity, P. A. *et al. Drosophila* photoreceptor axon guidance and targeting requires the dreadlocks SH2/SH3 adapter protein. *Cell* **85,** 639–650 (1996).
13. Lu, W., Katz, S., Gupta, R. & Mayer, B. J. Activation of Pak by membrane localization mediated by an SH3 domain from the adaptor protein Nck. *Curr. Biol.* **7,** 85–94 (1997).
14. Chen, M., She, H., Kim, A., Woodley, D. T. & Li, W. Nck-beta adapter regulates actin polymerization in NIH 3T3 fibroblasts in response to platelet-derived growth factor bb. *Mol. Cell. Biol.* **20,** 7867–7880 (2000).
15. Ren, R., Mayer, B. J., Cicchetti, P. & Baltimore, D. Identification of a ten-amino acid proline-rich SH3 binding site. *Science* **259,** 1157–1161 (1993).
16. Wunderlich, L., Farago, A. & Buday, L. Characterization of interactions of Nck with Sos and dynamin. *Cell Signal* **11,** 25–29 (1999).
17. Hobert, O., Jallal, B., Schlessinger, J. & Ullrich, A. Novel signaling pathway suggested by SH3 domain-mediated p95vav/heterogeneous ribonucleoprotein K interaction. *J. Biol. Chem.* **269,** 20225–20228 (1994).
18. Bustelo, X. R., Suen, K. L., Michael, W. M., Dreyfuss, G. & Barbacid, M. Association of the vav proto-oncogene product with poly(rC)-specific RNA-binding proteins. *Mol. Cell. Biol.* **15,** 1324–1332 (1995).
19. Ribon, V., Herrera, R., Kay, B. K. & Saltiel, A. R. A role for CAP, a novel, multifunctional Src Homology 3 domain-containing protein in formation of actin stress fibers and focal adhesions. *J. Biol. Chem.* **273,** 4073–4080 (1998).
20. Mandai, K. *et al.* Ponsin/SH3P12: an l-afadin- and vinculin-binding protein localized at cell–cell and cell–matrix adherens junctions. *J. Cell Biol.* **144,** 1001–1017 (1999).
21. Kurakin, A., Hoffman, N. G. & Kay, B. K. Molecular recognition properties of the C-terminal SH3 domain of the Cbl associated protein, CAP. *J. Pept. Res.* **52,** 331–337 (1998).
22. Zeng, L. *et al.* The mouse Fused locus encodes Axin, an inhibitor of the Wnt signaling pathway that regulated embryonic axis formation. *Cell* **90,** 181–192 (1997).
23. Ikeda, S. *et al.* Axin, a negative regulator of the Wnt signaling pathway, forms a complex with GSK-3β and β-catenin and promotes GSK-3β-dependent phosphorylation of β-catenin. *EMBO J.* **17,** 1371–1384 (1998).
24. Hamada, F. *et al.* Negative regulation of Wingless signaling by D-axin, a *Drosophila* homolog of axin. *Science* **283,** 1739–1742 (1999).
25. Fradkin, L. G., Noordermeer, J. N. & Nusse, R. The *Drosophila* Wnt protein DWnt-3 is a secreted glycoprotein localized on the axon tracts of the embryonic CNS. *Dev. Biol.* **168,** 202–213 (1995).
26. Asakura, T. *et al.* Similar and differential behavior between the nectin-afadin-ponsin and cadherin-catenin systems during the formation and disruption of the polarized junctional alignment in epithelial cells. *Genes Cells* **4,** 573–581 (1999).
27. Loureiro, J. & Peifer, M. Roles of Armadillo, a *Drosophila* catenin, during central nervous system development. *Curr. Biol.* **8,** 622–632 (1998).
28. Dai, Z. & Pendergast, A. M. Abi-2, a novel SH3-containing protein interacts with the c-Abl tyrosine kinase and modulates c-Abl transforming activity. *Genes Dev.* **9,** 2569–2582 (1995).
29. Shi, Y., Alin, K. & Goff, S. P. Abl-interactor-1, a novel SH3 protein binding to the carboxy-terminal portion of the Abl protein, suppresses v-abl transforming activity. *Genes Dev.* **9,** 2583–2597 (1995).
30. Keegan, K. & Cooper, J. A. Use of the two hybrid system to detect the association of the protein-tyrosine phosphatase, SHPTP2, with another SH2-containing protein, Grb7. *Oncogene* **12,** 1537–1544 (1996).
31. Schlaepfer, D. D., Hauck, C. R. & Sieg, D. J. Signaling through focal adhesion kinase. *Prog. Biophys. Mol. Biol.* **71,** 435–478 (1999).

Supplementary information is available on *Nature*'s World-Wide Web site (http://www.nature.com) or as paper copy from the London editorial office of *Nature*.

Acknowledgements

We thank T. Saxton and T. Pawson for numerous discussions; B. Howell, S. Hollenberg and J. Cooper for two-hybrid vectors and brain library; F. Gertler for CAP peptide spots; K. Womak, X. Cao and S. Kennedy for help with two-hybrid screens; and J. Shay for technical assistance. These studies were made possible by a grant from the Welch Foundation (to M.H.).

Correspondence and requests for materials should be addressed to M.H. (e-mail: henk@utsw.swmed.edu).

CREB regulates hepatic gluconeogenesis through the coactivator PGC-1

Stephan Herzig*, Fanxin Long*†, Ulupi S. Jhala*, Susan Hedrick*, Rebecca Quinn‡, Anton Bauer§, Dorothea Rudolph§, Gunther Schutz§, Cliff Yoon‖, Pere Puigserver‖, Bruce Spiegelman‖ & Marc Montminy*

** Peptide Biology Laboratories, Salk Institute for Biological Studies, 10010 N Torrey Pines Road, La Jolla, California 92037-1002, USA*
‡ Joslin Diabetes Center, Boston, Massachusetts 02215, USA
§ Molecular Biology of the Cell I, Deutsches Krebsforschungszentrum Im Neuenheimerfeld 280, D-69120 Heidelberg, Germany
‖ Dana-Farber Cancer Center, Department of Cell Biology, Harvard Medical School, Boston, Massachusetts 02115, USA

When mammals fast, glucose homeostasis is achieved by triggering expression of gluconeogenic genes in response to glucagon and glucocorticoids. The pathways act synergistically to induce gluconeogenesis (glucose synthesis), although the underlying mechanism has not been determined[1–4]. Here we show that mice carrying a targeted disruption of the cyclic AMP (cAMP) response element binding (CREB) protein gene, or overexpressing a dominant-negative CREB inhibitor, exhibit fasting hyperglycaemia and reduced expression of gluconeogenic enzymes. CREB was found to induce expression of the gluconeogenic programme through the nuclear receptor coactivator PGC-1, which is shown here to be a direct target for CREB regulation *in vivo*. Overexpression of PGC-1 in CREB-deficient mice restored glucose homeostasis and rescued expression of gluconeogenic genes. In transient assays, PGC-1 potentiated glucocorticoid induction of the gene for phosphoenolpyruvate carboxykinase (PEPCK), the rate-limiting enzyme in gluconeogenesis. PGC-1 promotes cooperativity between cyclic AMP and glucocorticoid signalling pathways during hepatic gluconeogenesis. Fasting hyperglycaemia is strongly correlated with type II diabetes, so our results suggest that the activation of PGC-1 by CREB in liver contributes importantly to the pathogenesis of this disease.

Cyclic AMP regulates the expression of numerous genes through phosphorylation of CREB at Ser 133, mediated by protein kinase A (PKA)[5]. The ability of CREB to stimulate the gluconeogenic PEPCK gene[6,7] prompted us to examine the general importance of this factor for activation of the gluconeogenic programme under fasting conditions. We generated transgenic mice expressing a dominant negative CREB protein, referred to as A-CREB, under control of the liver-specific albumin promoter/enhancer[8]. A-CREB contains the leucine zipper of CREB plus an acidic extension that enhances the

† Present address: Department of Molecular and Cellular Biology, The Biolabs, Harvard University, Cambridge, Massachusetts 02138, USA.

affinity for, and disrupts the DNA-binding activity of, CREB family members (CREB, CREM, ATF-1) but not other bZIP proteins[9,10]. The CRE-binding activity of CREB was reduced by 80% in liver nuclear extracts from A-CREB transgenic mice compared with wild-type littermates, as measured by a gel mobility shift assay (Fig. 1a, compare lanes 2 and 4), despite comparable levels of full-length CREB protein, as shown by a western blot assay (Fig. 1a, bottom). A-CREB mice were profoundly hypoglycaemic (Fig. 1b), and RNA levels for the gluconeogenic enzymes PEPCK and glucose-6-phosphatase (G6Pase) in the liver were lower in these animals than in wild-type littermates (Fig. 1c).

To evaluate acute effects of CREB activity on glucose homeostasis, we prepared an adenovirus expressing A-CREB under the control of the cytomegalo virus (CMV) promoter. Following systemic injection of either A-CREB or control adenovirus, 80–90% of hepatocytes in livers of 6-week-old male mice were infected as determined by visible fluorescence from a co-expressed green fluorescent protein (GFP) marker (not shown). In the fed state, blood glucose levels in A-CREB-infected mice were comparable to those of mice infected with control virus (Fig. 2a; 1.04 ± 0.10 mg ml^{-1} and 1.35 ± 0.20 mg ml^{-1} (mean ± s.e.m.) at day 8, respectively). During the fasting period, however, glucose levels were far lower in A-CREB mice than in control injected mice (0.65 ± 0.04 mg ml^{-1} and 1.38 ± 0.05 mg ml^{-1} at day 8, respectively), demonstrating that CREB activity is required to mobilize glucose via the gluconeogenic pathway (Fig. 2a). Indeed, expression of the PEPCK, G6Pase and pyruvate carboxylase genes was reduced fourfold in livers of A-CREB mice compared with control mice (Fig. 2b). Blood insulin levels in control and A-CREB mice were comparable in both fed and fasted states (see Supplementary Information Fig. 1).

Fasting hyperglycaemia is strongly correlated with insulin resistance in type II diabetic patients[11]. To test the role of CREB in hepatic glucose production in this setting, we employed *db*/*db* diabetic mice, which display adult-onset diabetes owing to a mutation in the leptin receptor gene[12,13]. Compared with wild-type mice, blood glucose levels in *db*/*db* mice were significantly elevated in both the fed and fasted states (Fig. 2c; 2.70 ± 0.17 mg ml^{-1} (fed) and 2.50 ± 0.16 mg ml^{-1} (fasted) at day 7). At the same time, PEPCK messenger RNA levels were 2.5-fold higher in fasted *db*/*db* mice than in wild-type mice (Fig. 2d, compare bars 1 and 3). After injection with A-CREB virus, the blood glucose levels of fasted *db*/*db* mice returned to normal (Fig. 2c, 1.22 ± 0.09 mg ml^{-1} at day 7) as did PEPCK mRNA levels (Fig. 2d, bar 2). In parallel, plasma insulin levels in fasting *db*/*db* mice decreased 40% after injection of A-CREB adenovirus (see Supplementary Information Fig. 1).

The reduced expression of G6Pase and pyruvate carboxylase genes in A-CREB-expressing mice is consistent with the hypoglycaemic effects of A-CREB during fasting; disruption of either gene leads to severe hypoglycaemia[14,15]. Remarkably, the G6Pase promoter lacks a discernible CRE[16] and the pyruvate carboxylase gene contains only a weak CRE half-site[17], suggesting an indirect role for CREB in the regulation of both genes. Expression of PGC-1 has been found to be induced in diabetes and to stimulate gluconeogenic enzymes in cultured hepatocytes[18], prompting us to examine the role of PGC-1 in mediating CREB signalling under fasting conditions *in vivo*.

Levels of PGC-1 mRNA in normal adult liver were elevated fourfold after 8 h of food restriction (Fig. 2d, compare bars 6 and 7); and expression of A-CREB blocked PGC-1 induction (Fig. 2b). Consistent with the fasting hyperglycaemia in *db*/*db* mice, PGC-1 mRNA levels were induced threefold in *db*/*db* compared with wild-type mice (Fig. 2d, compare bars 4 and 6); overexpression of A-CREB reduced PGC-1 mRNA levels to normal (Fig. 2d, bar 5). Sequence analysis of the mouse PGC-1 promoter revealed a full palindromic consensus CRE centred at −130 (Fig. 3a). To determine whether PGC-1 is indeed a direct target for CREB action *in vivo*, we performed chromatin immunoprecipitation studies using HepG2 hepatoma cells. The PGC-1 promoter was efficiently recovered from immunoprecipitates of CREB but not of control immunoglobulin-γ (IgG) (Fig. 3a, compare lanes 3–5). Confirming the specificity of these antisera, no polymerase chain reaction (PCR) product was obtained from CREB immunoprecipitates using control glyceraldehyde-3-phosphate dehydrogenase (GAPDH) primers (Fig. 3a, lanes 3–5).

In transient assays of HepG2 hepatoma cells, PGC-1 promoter activity was induced 3–4-fold by a cAMP agonist (Fig. 3b). Co-transfection of an A-CREB expression vector blocked induction of the PGC-1 promoter by cAMP, demonstrating that PGC-1 is indeed a direct target for CREB activity in hepatocytes (Fig. 3b). Consistent with downregulation of PGC-1 under feeding conditions, PGC-1 reporter activity was blocked in cells treated with insulin (Fig. 3b). The half-maximal dose for inhibition of endogenous PGC-1 mRNA (0.1–0.5 nM) was within the physiologic range of insulin concentrations (see Supplementary Information Fig. 2). In keeping with the rapid effects of insulin on hepatic gene expression, PGC-1 mRNA levels were reduced by 70% within 30 min of treatment (see Supplementary Information Fig. 2).

The ability of cAMP to induce a nuclear receptor coactivator in liver prompted us to speculate that PGC-1 promotes cooperativity between cAMP and glucocorticoid pathways during fasting. Towards this end, we co-infected mice with A-CREB and PGC-1 adenovirus constructs. Whereas A-CREB adenovirus alone induced hypoglycaemia in fasted mice, co-infection with PGC-1 adenovirus restored fasting glucose levels to near normal (Fig. 3c) and rescued gluconeogenic gene expression (data not shown). Arguing against

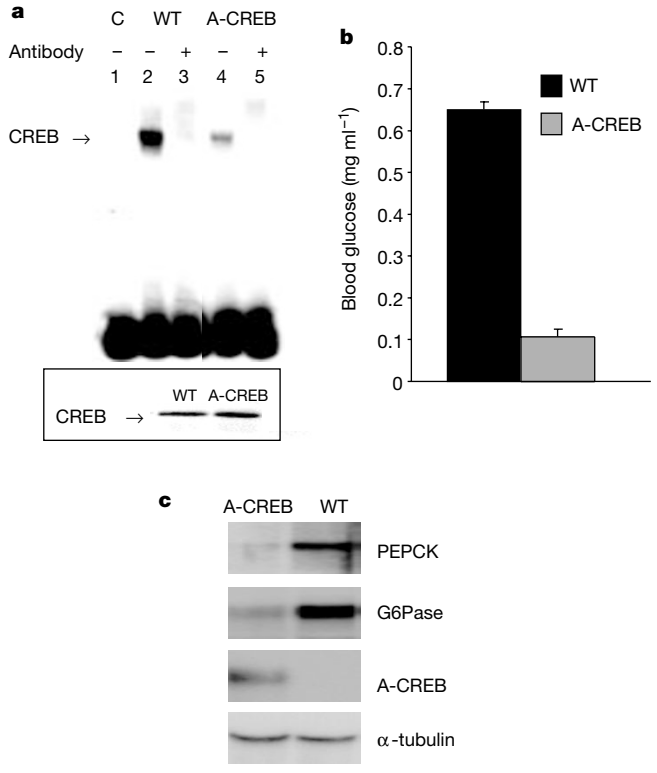

Figure 1 Transgenic mice expressing a dominant negative CREB inhibitor in liver display profound hypoglycaemia at birth. **a**, Top, gel mobility shift assay of liver nuclear extracts from newborn A-CREB transgenic mice and wild-type (WT) littermates using ^{32}P-labelled CRE oligonucleotide. Bottom, Western blot of liver nuclear extracts from wild-type and A-CREB transgenic mice using anti-CREB antiserum 244. **b**, Blood glucose measurements of A-CREB transgenic and wild-type littermates at birth before feeding (mean ± s.e.m., $n = 5$ per group). **c**, Northern blot analysis of PEPCK, G6Pase, A-CREB and tubulin RNAs in livers from wild-type and A-CREB transgenic mice.

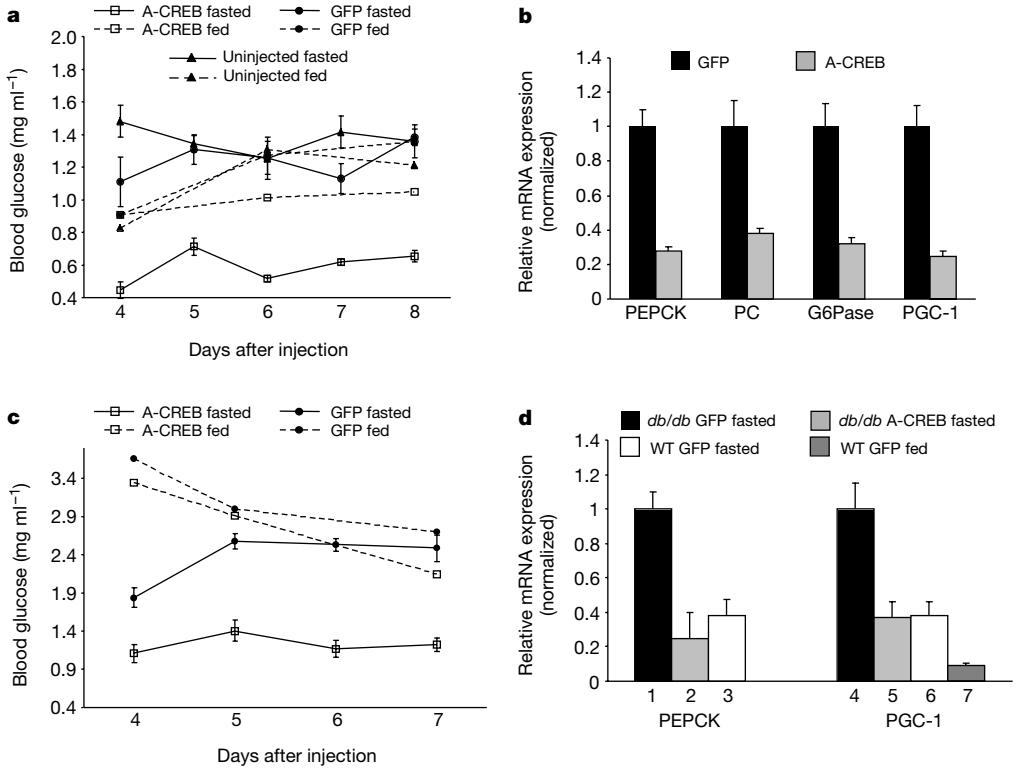

Figure 2 CREB activity is required for glucose homeostasis during fasting. **a**, Blood glucose levels in 6-week-old male mice ($n = 6$ per group) injected with control (GFP) adenovirus or A-CREB adenovirus, or left uninjected, under fed or fasted (9 h) conditions. **b**, Levels of mRNA for PEPCK, G6Pase and pyruvate carboxylase (PC) in livers ($n = 3$ per group) from control (GFP) and A-CREB adenovirus-infected fasting mice. **c**, Blood glucose levels in *db*/*db* diabetic mice infected with control (GFP) and A-CREB viruses as in **a**. **d**, PEPCK and PGC-1 mRNA levels in fed and fasted mice injected with control (GFP) or A-CREB viruses. Data are means ± s.e.m.

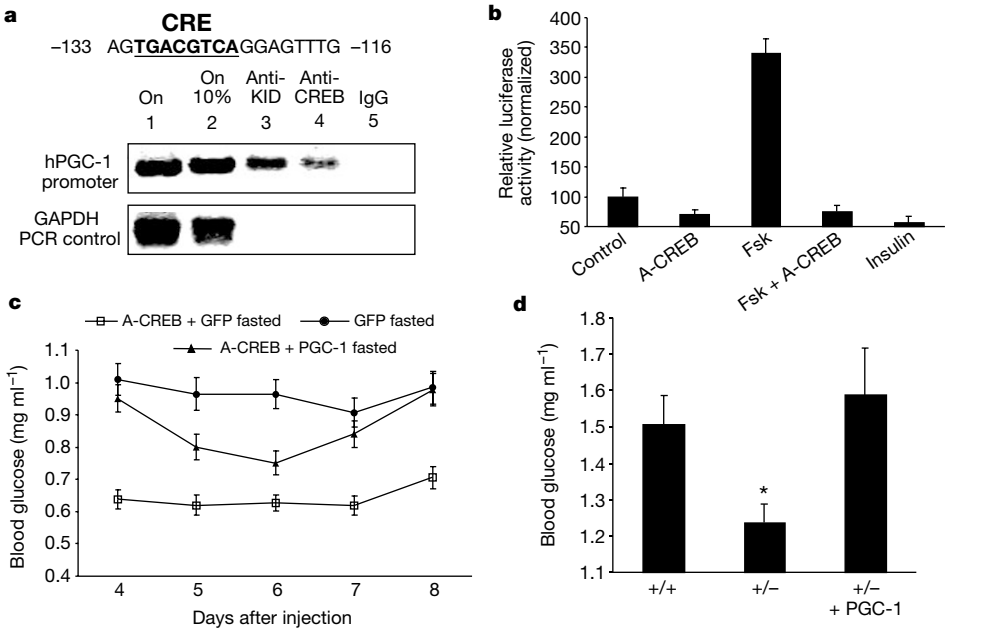

Figure 3 CREB promotes hepatic gluconeogenesis through PGC-1 during fasting. **a**, Chromatin immunoprecipitation assay of HepG2 cells using CREB-specific antisera (anti-KID, anti-CREB). PCR amplification products from reactions with human PGC-1 promoter (–170 to +68) or GAPDH coding region (+586 to +1037) primers. Lanes 1 and 2, onput controls. Lanes 3 and 4, PCR products obtained from immunoprecipitates of CREB using antisera specific for anti-KID (amino acids 100–160) and anti-CREB (amino acids 1–341). Lane 5, control immunoprecipitation with non-specific IgG. The PGC-1 promoter CRE element is shown above. **b**, Transient assay of HepG2 cells transfected with PGC-1 luciferase reporter (–170 to +68) and treated with forskolin (Fsk, 10 μM), A-CREB expression vector or insulin. **c**, Glucose levels of fasting mice injected with GFP, A-CREB plus GFP, or A-CREB plus PGC-1 adenoviruses. **d**, Glucose levels in fasting $CREB^{+/-}$ and wild-type littermates infected with GFP or PGC-1 virus for 8 days. Data are means ± s.e.m. Asterisk, $P < 0.05$ ($n = 5$).

a non-specific effect of PGC-1 on A-CREB expression, levels of the A-CREB inhibitor protein were identical in mice injected with A-CREB plus PGC-1 viruses and in mice injected with A-CREB alone (see Supplementary Information Fig. 3).

To test further the importance of PGC-1 in promoting hepatic gluconeogenesis through CREB, we employed $CREB^{+/-}$ mice[19]. $CREB^{+/-}$ heterozygotes had lower fasting blood glucose levels than wild-type littermates (Fig. 3d); and injection of PGC-1 adenovirus corrected the relative glucose imbalance in fasted $CREB^{+/-}$ mice, revealing the ability of this coactivator to act downstream of CREB to promote hepatic gluconeogenesis (Fig. 3d).

To determine the mechanism by which PGC-1 regulates expression of gluconeogenic genes, we performed transient assays of HepG2 cells using a PEPCK reporter plasmid. Treatment with a cAMP agonist stimulated PEPCK promoter activity 3–4-fold (Fig. 4a); and, consistent with the presence of a consensus CRE sequence in the PEPCK promoter[20], co-transfection of A-CREB inhibitor plasmid blocked reporter induction (Fig. 4a). Overexpression of PGC-1 potentiated cAMP-dependent induction of a −490 PEPCK promoter construct in HepG2 cells, but had no effect on a −355 PEPCK reporter lacking the glucocorticoid response unit (GRU; −455 to −340) (Fig. 4b). The GRU consists of binding sites for the glucocorticoid receptor plus additional transcription factors such as HNF-4 and HNF-3 that collectively mediate induction of the PEPCK promoter in response to glucocorticoids and insulin resistance[21,22].

The ability of PGC-1 to interact with, and potentiate the activity of, the glucocorticoid receptor[23] prompted us to examine the effect of PGC-1 on induction of the PEPCK promoter by glucocorticoids. Dexamethasone treatment or PGC-1 overexpression alone had little effect on PEPCK promoter activity in HepG2 cells (Fig. 4a), but co-transfection of PGC-1 expression vector strongly induced −490 PEPCK promoter activity in response to dexamethasone (Fig. 4a). Supporting a GRU-dependent mechanism of activation, PGC-1 had no effect on a PEPCK reporter construct lacking the GRU (−355 PEPCK) in cells treated with either dexamethasone or cAMP agonist (Fig. 4b).

Our results argue for a two-step model in the activation of gluconeogenic genes by CREB during fasting (Fig. 4c). Ser 133 phosphorylation of CREB in response to catecholamine and glucagon stimulation during the early fasting period induces certain gluconeogenic enzymes (PEPCK) through a direct CREB-mediated effect. Under prolonged fasting, CREB further potentiates gluconeogenic genes (PEPCK, pyruvate carboxylase and G6Pase) by inducing expression of the coactivator PGC-1 in liver. PGC-1 then mediates activation of the gluconeogenic programme in response to glucocorticoid signals. This model is consistent with the observation that the GRU in the PEPCK gene is abnormally activated in type II diabetes, and that treatment with glucocorticoid antagonist reduces blood glucose levels in *db*/*db* diabetic mice[22].

The effect of A-CREB on liver gene expression suggests that CREB may constitute an ideal target for therapeutic intervention. Although use of a dominant negative inhibitor such as A-CREB may not be feasible in this regard, small molecules that block CREB phosphorylation or disrupt recruitment of the CREB coactivator CBP (CREB binding protein) may prove effective. Such compounds may be particularly beneficial as adjunctive therapy in lowering fasting blood glucose levels in type II diabetics. □

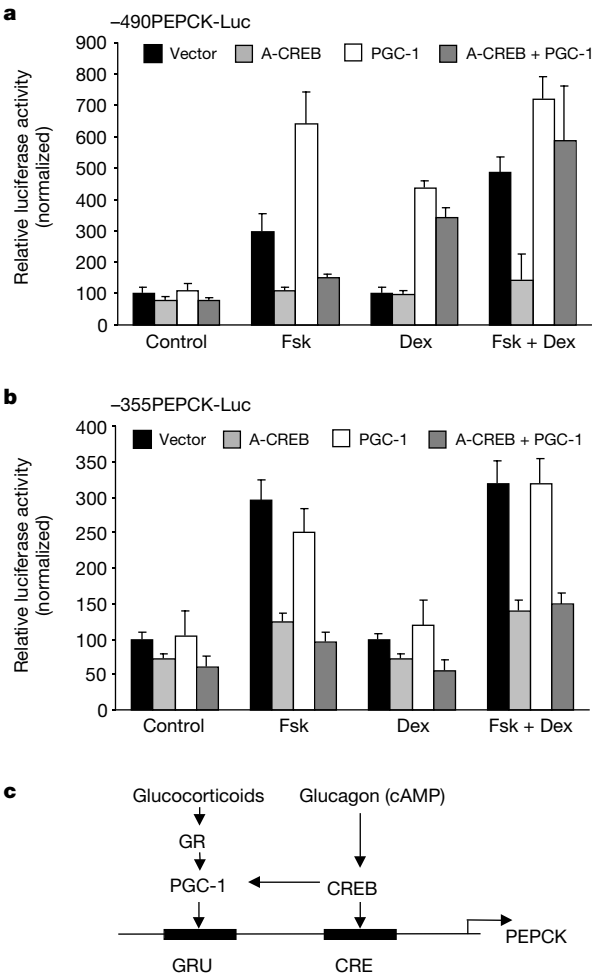

Figure 4 PGC-1 mediates induction of the PEPCK gene through the GRU. Transient assay of HepG2 hepatoma cells transfected with PEPCK luciferase reporter vectors either (**a**) containing (−490) or (**b**) lacking (−355) the GRU. Treatment with forskolin (Fsk, 10 μM) and/or dexamethasone (Dex, 10^{-7} M) is indicated. The effect of PGC-1 and A-CREB vectors on PEPCK promoter activity is shown. Data are means ± s.e.m. **c**, Model for cooperation between PGC-1 and CREB on the PEPCK promoter. CREB stimulates the PEPCK promoter activity directly through a consensus CRE and indirectly through induction of PGC-1, which induces the GRU through interaction with the glucocorticoid receptor (GR).

Methods

Recombinant adenoviruses

Adenoviruses expressing either A-CREB or PGC-1 were generated through homologous recombination between a linearized transfer vector pAD-Track and the adenoviral backbone vector pAD-Easy as described[24]. pAD-A-CREB contained a *Not*I/*Spe*I fragment from ZEO-A-CREB encoding a Flag-tagged A-CREB polypeptide[25]. pAD-PGC-1 carried the entire murine PGC-1 complementary DNA encoding all but the carboxy-terminal four amino acids. Both viruses co-expressed the GFP transcribed from a second independent CMV promoter to monitor viral infection efficiency. Adenovirus coding for GFP only (pAD-GFP) was used as a control in all experiments. Viruses were purified by the CsCl method and dialysed against PBS buffer containing 10% glycerol before animal injections as described[26].

Animal experiments

Male 6-week-old C57Bl6 or *db*/*db* mice were obtained from The Jackson Laboratory and maintained on a 12-h light–dark cycle with regular unrestricted diet. For virus injections, animals were anaesthetized with Iso-Flurane and a total of 1×10^9 plaque-forming units per recombinant virus was administered by a systemic tail vein injection. In each experiment at least six animals received identical treatments. Animals were fasted for 9–18 h overnight with free access to water. Blood glucose was monitored at the end of each fasting period for at least seven consecutive days. Blood glucose was also measured in the non-fasted state immediately before food withdrawal. Blood samples were collected from the tail vein. Liver tissue for RNA and protein isolation was immediately frozen in liquid nitrogen. Additional liver samples were fixed in 10% formaldehyde, sectioned with a cryomicrotome, and investigated for viral infection efficiency by fluorescence microscopy. Studies with CREB knockout mice carrying a targeted disruption of the CREB DNA-binding domain and leucine zipper region[19] were performed as described above.

Blood metabolites

Blood glucose values were determined from whole blood using an automatic glucose monitor (One Touch, Lifescan). Plasma insulin levels were determined using a commercial insulin enzyme-linked immunosorbent assay kit (Crystal Chem).

TaqMan and northern blot analyses

PolyA$^+$ RNA and total RNA were extracted from homogenized mice livers using the Fast Track 2.0 (Invitrogen) or the RNeasy (Qiagen) kit. RNA samples were treated with DNase I (Promega) and RNA quality was assessed by gel electrophoresis. cDNA was prepared by reverse transcription of 250 ng mRNA or 500 ng total RNA using the Superscript II enzyme and Oligo dT primer (GIBCO BRL). The resulting cDNAs were amplified using the SYBR green PCR kit and an ABIPRISM 7700 Sequence detector (Perkin Elmer). All mRNA expression data from the TaqMan PCR with reverse transcription was normalized to GAPDH expression in the corresponding sample. Northern blot assays were performed as previously described[25].

Protein analysis

Protein was extracted from frozen liver samples in SDS-urea-lysis buffer and 20 μg of protein were loaded onto a 12% SDS–polyacrylamide gel and blotted onto nitrocellulose membrane. Western blot assays were performed as previously described[25].

Chromatin immunoprecipitation assay

Human hepatoma HepG2 cells were grown to 90% confluence, and the chromatin immunoprecipitation assay was performed as described elsewhere[27]. Specific antibodies against either full-length CREB (253) or the kinase inducible domain (KID) (244) of CREB were used for the immunoprecipitation. Normal rabbit IgG served as a negative control. Precipitated DNA fragments were analysed by PCR amplification using primers directed against the human PGC-1 promoter region, or the GAPDH coding region as negative control.

Plasmids

Expression plasmids pZEO-A-CREB[25] and pcDNA3-PGC-1[28] have been described previously. The liver-specific A-CREB transgene was constructed by inserting A-CREB cDNA into a liver-specific albumin promoter/enhancer plasmid[8]. To construct luciferase expression plasmids −490PEPCK-Luc and −355PEPCK-Luc *Bam*HI/*Bgl*II fragments of the PEPCK promoter region containing 490 or 355 base pairs (bp) of the mouse PEPCK 5′-flanking region, respectively, were cloned into the pGL3 basic luciferase reporter vector (Promega). PGC-1 reporter mPGC-Luc was constructed by inserting a 230-bp fragment of the mouse PGC-1 promoter containing 170 bp of the 5′-flanking region and 68 bp of exon 1 into the pGL3 vector.

Cell culture and transfection assays

Human hepatoma HepG2 cells were transfected using the Lipofectamine 2000 reagent (GIBCO BRL) according to the manufacturer's instructions (500 ng of indicator plasmid per well). Where indicated, expression plasmids encoding A-CREB (pZeo-A-CREB)[25] or PGC-1 (pcDNA3-PGC-1)[28] were cotransfected (50 ng and 800 ng plasmid per well, respectively). Cotransfections were performed with a constant amount of DNA by adding the empty pcDNA3 vector (Invitrogen). Cells were treated with forskolin (10 μM) and/or dexamethasone (100 nM) or insulin (100 nM) for 14 h. Cell extracts were prepared 48 h after transfection and the luciferase assay was performed as described previously[29], normalizing to activity from cotransfected Rous sarcoma virus-β-galactosidase expression plasmid (100 ng plasmid per well).

Received 29 May; accepted 25 July 2001.

1. Hanson, R. W. & Reshef, L. Regulation of phosphoenolpyruvate carboxykinase (GTP) gene expression. *Annu. Rev. Biochem.* **66,** 581–611 (1997).
2. Lemaigre, F. P. & Rousseau, G. G. Transcriptional control of genes that regulate glycolysis and gluconeogenesis in adult liver. *Biochem. J.* **303,** 1–14 (1994).
3. Angrand, P. O., Coffinier, C. & Weiss, M. C. Response of the phosphoenolpyruvate carboxykinase gene to glucocorticoids depends on the integrity of the cAMP pathway. *Cell Growth Differ.* **5,** 957–966 (1994).
4. Imai, E., Miner, J. N., Mitchell, J. A., Yamamoto, K. R. & Granner, D. K. Glucocorticoid receptor–cAMP response element-binding protein interaction and the response of the phosphoenolpyruvate carboxykinase gene to glucocorticoids. *J. Biol. Chem.* **268,** 5353–5356 (1993).
5. Gonzalez, G. A. & Montminy, M. R. Cyclic AMP stimulates somatostatin gene transcription by phosphorylation of CREB at Serine 133. *Cell* **59,** 675–680 (1989).
6. Liu, J. S., Park, E. A., Gurney, A. L., Roesler, W. J. & Hanson, R. W. Cyclic AMP induction of phosphoenolpyruvate carboxykinase (GTP) gene transcription is mediated by multiple promoter elements. *J. Biol. Chem.* **266,** 19095–19102 (1991).
7. Quinn, P. G. & Granner, D. K. Cyclic AMP-dependent protein kinase regulates transcription of the phosphoenolpyruvate carboxykinase gene but not binding of nuclear factors to the cyclic AMP regulatory element. *Mol. Cell. Biol.* **10,** 3357–3364 (1990).
8. Liu, J. K., Bergman, Y. & Zaret, K. S. The mouse albumin promoter and a distal upstream site are simultaneously DNase I hypersensitive in liver chromatin and bind similar liver-abundant factors in vitro. *Genes Dev.* **2,** 528–541 (1988).
9. Ahn, S. *et al.* A dominant negative inhibitor of CREB reveals that it is a general mediator stimulus-dependent transcription of c-*fos*. *Mol. Cell. Biol.* **18,** 967–977 (1998).
10. Long, F., Schipani, E., Asahara, H., Kronenberg, H. & Montminy, M. The CREB family of activators is required for endochondral bone development. *Development* **128,** 541–550 (2001).
11. Consoli, A. Role of liver in pathophysiology of NIDDM. *Diabetes Care* **15,** 430–441 (1992).
12. Lee, G. H. *et al.* Abnormal splicing of the leptin receptor in diabetic mice. *Nature* **379,** 632–635 (1996).
13. Chen, H. *et al.* Evidence that the diabetes gene encodes the leptin receptor: identification of a mutation in the leptin receptor gene in *db*/*db* mice. *Cell* **84,** 491–495 (1996).
14. Wexler, I. D. *et al.* Molecular characterization of pyruvate carboxylase deficiency in two consanguineous families. *Pediatr. Res.* **43,** 579–584 (1998).
15. Lei, K. J. *et al.* Glucose-6-phosphatase dependent substrate transport in the glycogen storage disease type-1a mouse. *Nature Genet.* **13,** 203–209 (1996).
16. Schmoll, D. *et al.* Identification of a cAMP response element within the glucose-6-phosphatase hydrolytic subunit gene promoter which is involved in the transcriptional regulation by cAMP and glucocorticoids in H4IIE hepatoma cells. *Biochem. J.* **338,** 457–463 (1999).
17. Jitrapakdee, S., Booker, G. W., Cassady, A. I. & Wallace, J. C. The rat pyruvate carboxylase gene structure. Alternate promoters generate multiple transcripts with the 5′-end heterogeneity. *J. Biol. Chem.* **272,** 20522–20530 (1997).
18. Yoon, J. C. *et al.* Control of hepatic gluconeogenesis through the transcriptional coactivator PGC-1. *Nature* **413,** 131–138 (2001).
19. Rudolph, D. *et al.* Impaired fetal T cell development and perinatal lethality in mice lacking the cAMP response element binding protein. *Proc. Natl Acad. Sci. USA* **95,** 4481–4486 (1998).
20. Short, J. M., Wynshaw-Boris, A., Short, H. P. & Hanson, R. W. Characterization of the phosphoenolpyruvate carboxykinase (GTP) promoter-regulatory region. II. Identification of cAMP and glucocorticoid regulatory domains. *J. Biol. Chem.* **261,** 9721–9726 (1986).
21. Imai, E. *et al.* Characterization of a complex glucocorticoid response unit in the phosphoenolpyruvate carboxykinase gene. *Mol. Cell. Biol.* **10,** 4712–4719 (1990).
22. Friedman, J. E. *et al.* Phosphoenolpyruvate carboxykinase (GTP) gene transcription and hyperglycemia are regulated by glucocorticoids in genetically obese *db*/*db* transgenic mice. *J. Biol. Chem.* **272,** 31475–31481 (1997).
23. Knutti, D., Kaul, A. & Kralli, A. A tissue-specific coactivator of steroid receptors, identified in a functional genetic screen. *Mol. Cell. Biol.* **20,** 2411–2422 (2000).
24. He, T. *et al.* A simplified system for generating recombinant adenoviruses. *Proc. Natl Acad. Sci. USA* **95,** 2509–2514 (1998).
25. Michael, L. F., Asahara, H., Shulman, A., Kraus, W. & Montminy, M. The phosphorylation status of a cyclic AMP-responsive activator is modulated via a chromatin-dependent mechanism. *Mol. Cell. Biol.* **20,** 1596–1603 (2000).
26. Becker, T. *et al.* Use of recombinant adenovirus for metabolic engineering of mammalian cells. *Methods Cell Biol.* **43,** 161–189 (1994).
27. Shang, Y., Hu, X., DiRenzo, J., Lazar, M. & Brown, M. Cofactor dynamics and sufficiency in estrogen receptor-regulated transcription. *Cell* **103,** 843–852 (2000).
28. Puigserver, P. *et al.* A cold-inducible coactivator of nuclear receptors linked to adaptive thermogenesis. *Cell* **92,** 829–839 (1998).
29. Nakajima, T. *et al.* RNA helicase A mediates association of CBP with RNA polymerase II. *Cell* **90,** 1107–1112 (1997).

Supplementary information is available on *Nature*'s World-Wide Web site (http://www.nature.com) or as paper copy from the London editorial office of *Nature*.

Acknowledgements

We thank J. Frangioni for help with adenovirus constructs, C. Arias for help with histology, and K. Suter for performing injections. This work was supported by grants from the National Institutes for Health to M.M. and from the DFG to S.H.

Correspondence and requests for materials should be addressed to M.M. (e-mail: montminy@salk.edu).

erratum

Roles of tumour localization, second signals and cross priming in cytotoxic T-cell induction

Adrian F. Ochsenbein, Sophie Sierro, Bernhard Odermatt, Marcus Pericin, Urs Karrer, Ian Hermans, Silvio Hemmi, Hans Hengartner & Rolf M. Zinkernagel

Nature **411,** 1058–1064 (2001).

In this Letter, the first name of Ian Hermans was misspelled as 'Jan'. □

ring trap. in *Proc. Workshop on Trapped Charged Particles and Fundamental Physics* (eds Dubin, D. & Schneider, D.) *AIP Conf. Proc.* **457,** 269–273 (1999).
12. Schramm, U., Schätz, T. & Habs, D. in *Proc. Conf. on Appl. of Acc. in Research and Industry* (eds Duggan, J. L.) *AIP Conf. Proc.* **576** (in the press).
13. Bryant, P. J. & Johnson, K. *Circular Accelerators and Storage Rings* (Cambridge Univ. Press, Cambridge, 1993).
14. Spreiter, Q., Seurer, M. & Toepffer, C. Relaxation in a strongly coupled particle beam. *Nucl. Instrum. Methods A* **364,** 239–242 (1995).
15. Seurer, M., Spreiter, Q. & Toepffer, C. in *Crystalline Beams and Related Issues* (eds Maletic, D. M. & Ruggiero, A. G.) 311–328 (World Scientific, Singapore, 1996).
16. Raizen, M. G. *et al.* Ionic crystals in a linear Paul trap. *Phys. Rev. A* **45,** 6493–6501 (1992).
17. Drewsen, M., Brodersen, C., Hornekaer, L., Hangst, J. S. & Schiffer, J. P. Large ion crystals in a linear Paul trap. *Phys. Rev. Lett.* **81,** 2878–2881 (1998).
18. Birkl, G., Kassner, S. & Walther, H. Multiple-shell structures of laser-cooled Mg-ions in a quadrupole storage ring. *Nature* **357,** 310–313 (1992).
19. Hasse, R. W. & Schiffer, J. P. The structure of the cylindrically confined Coulomb lattice. *Ann. Phys.* **203,** 419–448 (1990).
20. Habs, D. & Grimm, R. Crystalline ion beams. *Ann. Rev. Nucl. Part. Sci.* **45,** 391–428 (1995).
21. Schiffer, J. P. in *Crystalline Beams and Related Issues* (eds Maletic, D. M. & Ruggiero, A. G.) 217–228 (World Scientific, Singapore, 1996).
22. Wei, J., Okamoto, H. & Sessler, A. M. Necessary conditions for attaining a crystalline beam. *Phys. Rev. Lett.* **80,** 2606–2609 (1998).
23. Blümel, R. *et al.* Phase transitions of stored laser-cooled ions. *Nature* **334,** 309–313 (1988).
24. Dubin, D. H. E. First-order anharmonic correction to the free energy of a Coulomb-crystal in periodic boundary conditions. *Phys. Rev. A* **42,** 4972–4982 (1990).
25. Schiffer, J. P., Drewsen, M., Hangst, J. & Hornekaer, L. Temperature, ordering, and equilibrium with time-dependent forces. *Proc. Natl Acad. Sci. USA* **97,** 10697–10700 (2000).

Acknowledgements

We thank R. Neugart for technical support, and P. Kienle and H. Walther for discussions. The work was partially funded by the Deutsche Forschungsgemeinschaft and the Maier Leibmitz Labor.

Correspondence and requests for material should be addressed to U.S. (e-mail: ulrich.schramm@physik.uni-muenchen.de).

A titanosilicate molecular sieve with adjustable pores for size-selective adsorption of molecules

Steven M. Kuznicki*, Valerie A. Bell*, Sankar Nair†, Hugh W. Hillhouse†, Richard M. Jacubinas*, Carola M. Braunbarth†, Brian H. Toby‡ & Michael Tsapatsis†

** Strategic Technology Group, Engelhard Corporation, 101 Wood Avenue, Iselin, New Jersey 08830, USA*
† Department of Chemical Engineering, 159 Goessmann Laboratory, University of Massachusetts, Amherst, Massachusetts 01003, USA
‡ NIST Center for Neutron Research, National Institute of Standards and Technology, Gaithersburg, Maryland 20899-8562, USA

Zeolites and related crystalline microporous oxides—tetrahedrally coordinated atoms covalently linked into a porous framework—are of interest for applications ranging from catalysis to adsorption and ion-exchange[1]. In some of these materials (such as zeolite rho) adsorbates[2], ion-exchange, and dehydration and cation relocation[3,4] can induce strong framework deformations. Similar framework flexibility has to date not been seen in mixed octahedral/tetrahedral microporous framework materials, a newer and rapidly expanding class of molecular sieves[5–16]. Here we show that the framework of the titanium silicate ETS-4, the first member of this class of materials[8], can be systematically contracted through dehydration at elevated temperatures to 'tune' the effective size of the pores giving access to the interior of the crystal. We show that this so-called 'molecular gate' effect can be used to tailor the adsorption properties of the materials to give size-selective adsorbents[17] suitable for commercially important separations of gas mixtures of molecules with similar size in the 4.0 to 3.0 Å range, such as that of N_2/CH_4, Ar/O_2 and N_2/O_2.

ETS-4 has a mixed octahedral/tetrahedral framework (as shown in the diagram in Fig. 1) with a structure related to the mineral zorite[18–20], and has been described in terms of the random intergrowth of four hypothetical polymorphs[21]. Although larger openings are present in its structure, faulting ensures that access to the crystal interior of ETS-4 occurs through the relatively narrow eight-membered rings (8MRs), analogous to what is seen in small-pore zeolites[22]. The framework structure and cation positions of as-synthesized ETS-4 (Na-ETS-4) and of Sr-exchanged ETS-4 have been recently reported[21,23]. A distinct feature of ETS-4 is the presence of titania semioctahedra that are connected to framework silicon atoms through only four oxygen bridges[18,21], which gives rise to a planar connectivity, in contrast to the three-dimensional connectivity commonly encountered in other microporous frameworks.

As-synthesized ETS-4 has been reported to collapse near 200 °C to an amorphous material owing to the loss of structural water chains present along the channel system[15]. We found that carefully controlled heating leads to a monotonic decrease of the lattice dimensions in all three crystallographic directions, along with the gradual loss of crystallinity. Upon appropriate ion-exchange (for example, with Sr) the thermal stability of the structure, as inferred from diffraction and water adsorption measurements, can be extended to higher temperatures (for example, up to 350 °C for Sr-exchanged ETS-4).

Water-loss curves (as determined by thermal gravimetric analysis, TGA) for as-synthesized and Sr-exchanged ETS-4, along with representative room-temperature powder neutron diffraction patterns of Sr-exchanged ETS-4 after dehydration at temperatures up to 300 °C, are given in Fig. 2a and b, respectively. It is evident that the exchange by Sr leads to higher temperatures for dehydration, and as a result extends the stability range of the ETS-4 framework. The lattice constants, determined from the room-temperature neutron diffraction data, are listed in the Fig. 2 legend, while the evolution of these constants, as determined by *in situ* X-ray diffraction (XRD), is shown in Fig. 2c. A sharp structural transition takes place at ~110 °C, followed by a continuous contraction up to the point when the material becomes amorphous (at temperatures higher than 350 °C). We refer to the dehydrated materials as CTS (contracted titanosilicates). Samples of Sr-exchanged ETS-4 treated at temperatures higher than 250 °C exhibit increasing loss of order, as shown in the powder X-ray and neutron diffraction patterns. Reflections with a k component broaden and disappear first, indicating deformation and eventual breaking of the titania chains that run along the b axis.

The contraction of the CTS samples is preserved on cooling to room temperature in a dry environment. Samples treated at a temperature below 250 °C and rehydrated by exposure to moist air recover their original structure, as determined by XRD. The reversibility of the contraction/expansion phenomenon of ETS-4 points to the well known role of cation relocation on loss of water in inducing framework distortions[24–26]. Samples dehydrated at higher temperatures and exhibiting partial loss of X-ray crystallinity rehydrate more slowly, and do not fully recover their original crystalline structure upon rehydration. The unit cell dimensions of the partially disordered material produced by dehydration of Sr-exchanged ETS-4 at temperatures higher than 330 °C are stable upon exposure to moist air for at least two weeks. The irreversible change to the partially disordered structure (CTS) can be attributed to the destruction of connectivity of the titania chains and consequent loss of the restoring force needed to recover the original structure upon rehydration; strong cation coordination to framework oxygen atoms also promotes this irreversible change. Heat treatment at slightly higher temperatures (>350 °C) leads to complete loss of crystalline order.

Rietveld refinement[27–29] of the powder neutron diffraction data of Fig. 2b revealed a progressive and pronounced effect on the 8MR-opening in dehydrated samples (Fig. 3), in addition to cation

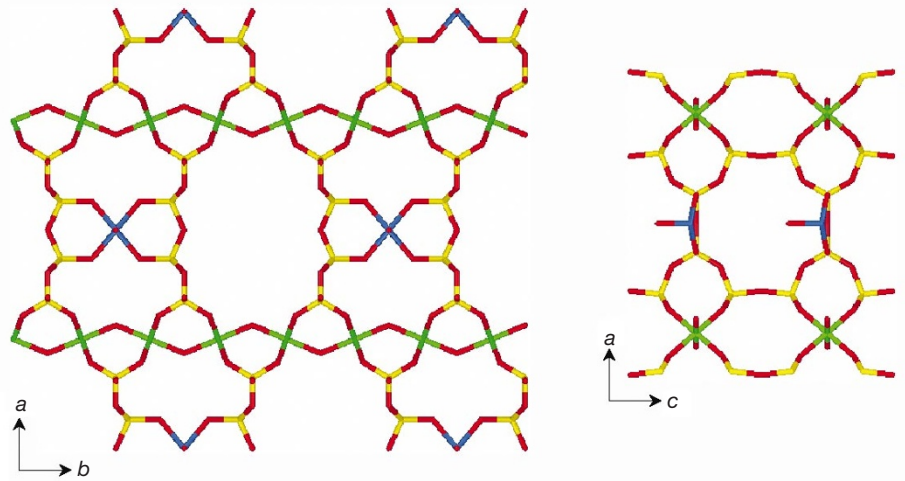

Figure 1 ETS-4 framework. Octahedrally coordinated titanium atoms that form O–Ti–O–Ti–O– chains along the *b* direction are shown in green. The titania semioctahedra of the bridging units that are connected to four framework silicon atoms through oxygen bridges are shown in blue. Silicon and oxygen atoms are shown in yellow and red, respectively. The *a*–*b* slice (left) shows the 12MR opening while the *a*–*c* slice (right) shows the 8MR opening. Pore connectivity along the *a* direction is through 6MRs. As a result, transport of molecules in ETS-4 can be considered to be two-dimensional within the *b*–*c* plane channel system. Owing to faulting, the connectivity of the 12MR down the *c* axis is interrupted and, therefore, transport and access to the interior of ETS-4 is controlled by the 8MR opening.

relocation. More specifically, with the contraction of the unit cell dimensions of ETS-4 during dehydration, the 8MR opening becomes asymmetric, with the D_1 distance (Fig. 3) decreasing monotonically. At the same time, cation relocation takes place and two new cation positions appear. One of the new cation positions (Sr3; see Supplementary Information Table I) is at the centre of the 8MR and its occupancy increases with the temperature of dehydration. Although this new cation position has a low occupancy, it nevertheless has pronounced effects on the access to the crystal interior owing to the two-dimensional connectivity of

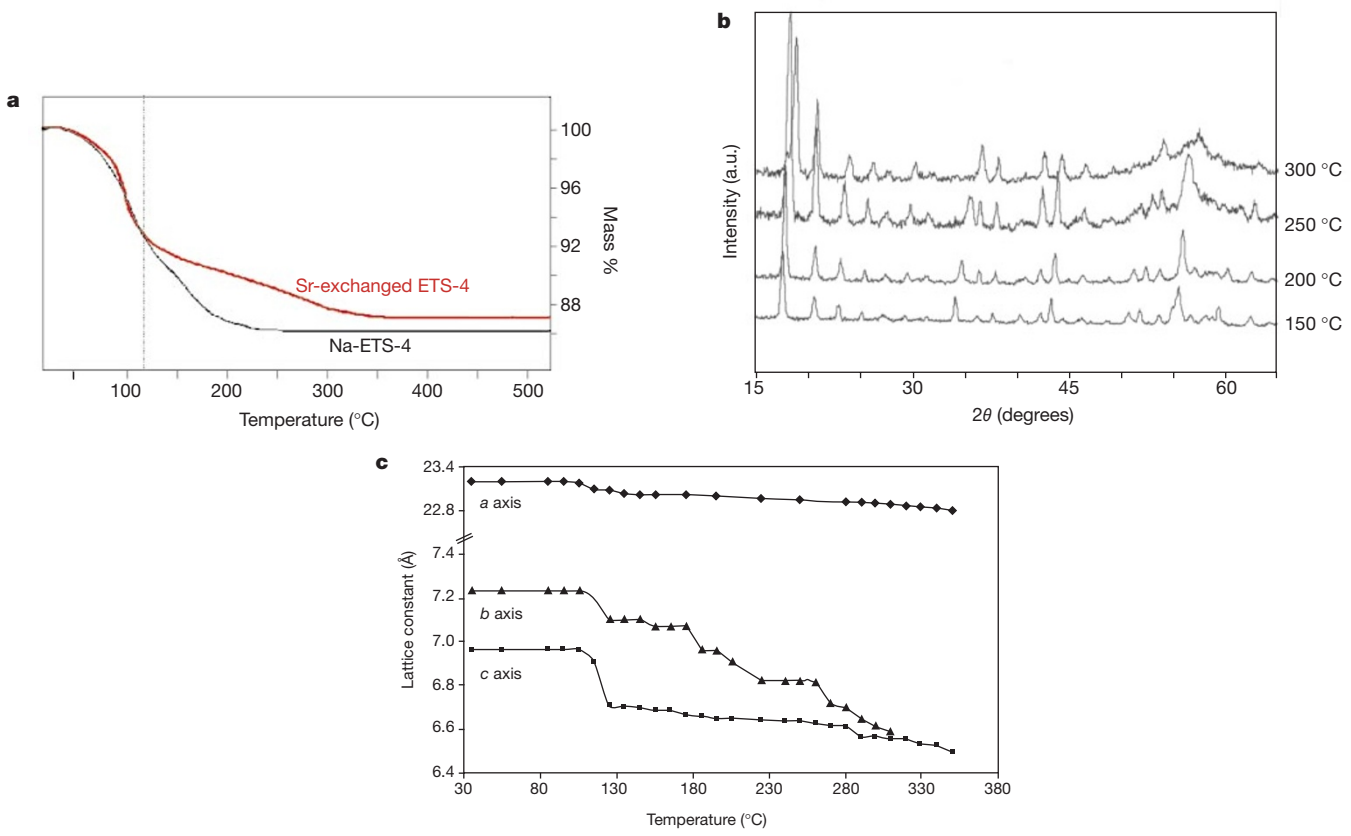

Figure 2 ETS-4 dehydration and associated decrease of the lattice constants. **a**, Thermogravimetric analysis (TGA) showing differences in the water loss of as-synthesized ETS-4 (Na-ETS-4) and Sr-exchanged ETS-4. **b**, Powder neutron diffraction patterns of Sr-exchanged ETS-4 collected at room temperature after dehydration at 150, 200, 250 and 300 °C. The corresponding lattice constants (*a* axis, *b* axis, *c* axis in Å) are: (23.0120, 7.0705, 6.6899), (23.0006, 6.9588, 6.6486), (22.9465, 6.8198, 6.6394), (22.9007, 6.6171, 6.5550) while the Le Bail weighted residuals (R_{wp}) are 1.68, 3.09, 3.41 and 3.56, respectively. The lattice parameters for the as-made sample are 23.1962, 7.2381, 6.965221. **c**, Changes of the lattice constants of Sr-exchanged ETS-4 during heat treatment as determined by *in situ* XRD.

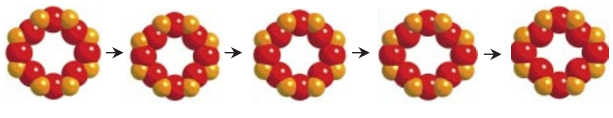

	RT	150°C	200°C	250°C	300°C
D_1(Å)	6.97 (4.27)	6.67 (3.97)	6.65 (3.95)	6.64 (3.94)	6.60 (3.90)
D_2(Å)	7.13 (4.43)	6.72 (4.02)	6.79 (4.09)	7.27 (4.57)	7.27 (4.57)
D_3(Å)	6.31 (3.61)	5.98 (3.28)	5.99 (3.29)	5.97 (3.27)	5.47 (2.77)

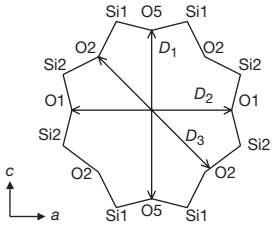

Figure 3 Reduction in the eight-membered ring (8MR) pore opening with increasing dehydration temperature. Oxygen to oxygen distances in the 8MR (D_1, D_2 and D_3) for the room-temperature structure of Sr-exchanged ETS-4 and for the samples dehydrated at 150, 200, 250 and 300 °C were calculated on the basis of atomic positions obtained from Rietveld refinements (see ref. 21, and Supplementary Information Table 1a–d and Fig. 1a–d). Oxygen atoms with identical labels are related by mirror planes. The O5–O5 (D_1) distance is equal to the lattice constant along *c* (see Fig. 2). The numbers in brackets are the effective distances obtained by subtracting twice the oxygen radius (1.35 Å; refs 30, 32) from the distances between the centres of the atoms. For a discussion of the size of the oxygen in molecular sieves, see ref. 32 and references therein. RT, room temperature.

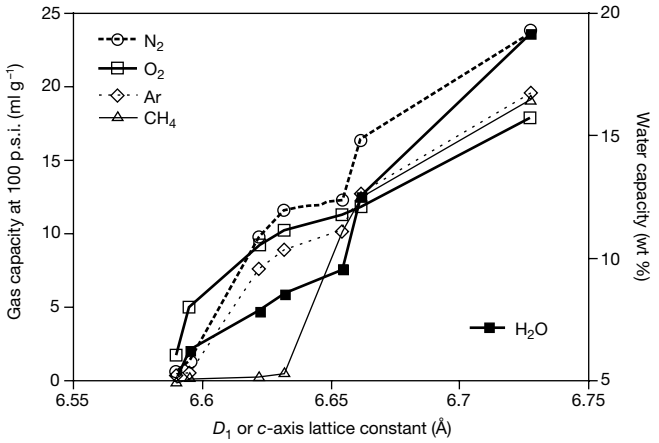

Figure 4 Sorption of molecules of various sizes with lattice contraction of Sr-exchanged ETS-4. This is the material used to provide the data in Figs 2 and 3; adsorption was performed at 25 °C for an equilibration time of 1 hour. 10-hour and 1-hour equilibrations yielded essentially identical results. The dehydration temperatures used to obtain the given D_1 values range from 150 to 350 °C. The corresponding Pauling dimensions[30] are: for CH_4, 4.2 Å; Ar, 3.84 Å; N_2, 4.1 Å (length), 3.00 Å (width); O_2, 3.9 Å (length), 2.8 Å (width); and H_2O, 3.9 Å (length), 3.15 Å (width).

the channel system of ETS-4 (Fig. 1). Both pore narrowing and cation relocation lead to a progressive reduction of the effective diameter of the 8MR.

The progressive contraction of the effective pore size of the 8MR opening profoundly affects the adsorption properties of these materials. Figure 4 shows a clear correlation between a measure of the 8MR opening and the material's adsorption capacity for various gas molecules. We note that although structure refinement of Sr-exchanged ETS-4 dehydrated at temperatures higher than 300 °C was not attempted owing to loss of crystallinity, the D_1 distance (see Fig. 3) of the 8MR opening coincides with the (001) *d*-spacing and can be reliably calculated from X-ray diffraction data. From Figs 2c, 3 and 4 it is evident that as dehydration temperature is increased and effective pore size[30] declines, molecules of progressively smaller dimensions are excluded from adsorption into the crystals.

This phenomenon, the contraction of the unit cell, is cation dependent. It occurs over the temperature regime associated with the loss of those crystal water molecules that are coordinated to the extra-framework cations. Other cation forms than those reported here show similar behaviour (for example, Ba-exchanged ETS-4); however, the specific cation or cation combination has a substantial effect on the temperature range over which shrinkage occurs. Partial exchange with Sr leads to similar behaviour, but the temperature range that leads to framework contraction through dehydration is larger. Figure 5 illustrates size-dependent separation of gas molecules using partially (75%) Sr-exchanged ETS-4 whose 8MR pores have been progressively contracted through dehydration. When the material is calcined at 190 °C, methane is readily adsorbed while the larger ethane molecules are essentially excluded. The capacity for methane absorption declines with further pore contraction; once the material has dehydrated at 270 °C, substantial exclusion occurs whereas the smaller nitrogen molecules are readily absorbed. Dehydration at 300 °C results in sufficiently pronounced pore contraction to show signs of nitrogen exclusion while smaller oxygen molecules can still penetrate the crystal, resulting in an oxygen-selective adsorbent. The dominant cause of loss of gas capacity for a species able to enter the crystal is reduction in crystallinity, with a lesser effect due to lattice shrinkage.

We refer to the ability to systematically manipulate the effective pore size in these materials as the 'molecular gate' effect, which enables the separation of molecules of nearly identical size. An important example is the separation of nitrogen from methane. Nitrogen occurs commonly in natural gas, to the extent that its presence can render many natural-gas reservoirs unusable. As Figs 4 and 5 illustrate, the effective ETS-4 pore size can be manipulated to exclude methane while still allowing the adsorption of the smaller nitrogen molecule. First field demonstrations show that the molecular gate phenomenon allows removal of nitrogen from natural gas (with water vapour contents of 80–150 p.p.m.) at well-head pressures, reducing an initial nitrogen content of 18% to less than 5% with a methane recovery of at least 90%[31]. The system consists of seven pressure-swing adsorption beds with overall process cycling time of 350 seconds, or 50 seconds adsorption per bed. On a laboratory scale, many other separations, including the major constituents of air (Ar/O_2 and N_2/O_2), have been accomplished[17].

The adsorption and structural results point to the contraction of the 8MRs and concomitant cation relocation as being primarily responsible for the gradual exclusion of smaller and smaller molecules. However, some contributions may be due to the presence and potential pore-blocking role of extra-framework species, which may result from the progressive loss of crystalline order that accompanies pore contraction. We have industrially manufactured ETS-4 on a multi-ton scale, using standard equipment and raw materials common to the zeolite industry. Despite the unit-cell contraction and disorder induced by dehydration, it retains adsorption capacities and uptake rates suitable for practical applications. For example, the adsorption step in removing nitrogen from natural gas can be completed in less than one minute. The kinetic stability of ETS-4 to rehydration allows the material to be used in relatively humid process streams. We have a pilot plant that has successfully purified methane using raw, wet natural gas for nearly two years. These features, and the ability to tune the effective pore size of ETS-4, make it an attractive system for a range of important and difficult gas separation applications. □

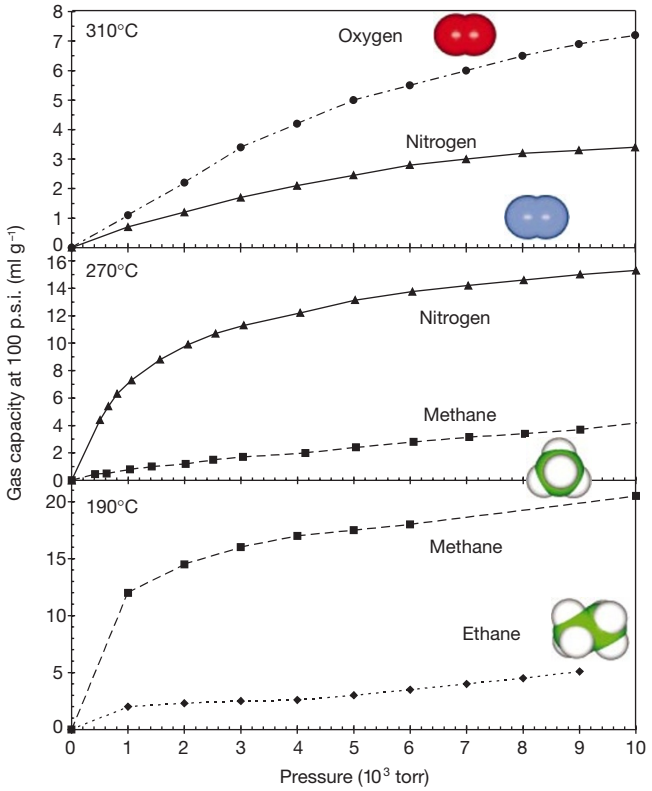

Figure 5 The molecular gate effect. Adsorption isotherms (collected at room temperature) for NaSr-ETS-4 (partially (75%) Sr-exchanged ETS-4) dehydrated at 190, 270 and 310 °C demonstrate that the corresponding CTS materials show selectivity for methane over ethane, nitrogen over methane and oxygen over nitrogen, respectively. The molecule shape illustrations were constructed using Mopac, as implemented in the Insight II (v4.0.0) software suite (Molecular Simulations Inc., San Diego, California, 1996).

Methods

Synthesis and characterization

ETS-4 synthesis and ion exchange were performed as described elsewhere[17,21]. *In situ* X-ray diffraction was performed using a Philips X'Pert diffractometer equipped with a high-temperature stage employing a Si internal standard. TGA was performed in a DSC/TGA (differential scanning calorimetry/thermogravimetric analysis) system with a heating rate of 0.5 °C min^{-1} in air and a flow rate of 10 litres per hour. ICP-MS (inductively coupled plasma-mass spectrometry) was used to determine the degree of ion-exchange. Adsorption data (Fig. 4) were collected in a VTI HPA-300 at 100 p.s.i. and 30 °C after dehydration for 24 h at the required temperature. Adsorption isotherms (Fig. 5) were collected, by VTI Corp., in a VTI HPA-300 at 25 °C, after 24 h of dehydration at the required temperature.

For the neutron diffraction studies, samples of Sr-exchanged ETS-4 were heat-treated at the required temperature for 24 h in Pyrex vials under dry helium flow. The vials were then sealed, isolated from the helium stream, and stored in a dry helium atmosphere. The samples were subsequently transferred to indium-sealed vanadium sample holders under a dry helium atmosphere. Neutron diffraction patterns were collected between 2θ values of 6° and 130° on the high-resolution BT-1 powder diffractometer at NIST (Gaithersburg, MD), operating at a wavelength of 2.0783 Å with a Ge(311) monochromator and a 15′ Soller collimator for high neutron flux.

Structure analysis

The room-temperature structure of Sr-ETS-4 in the *Cmmm* space group (solved from X-ray data) was taken as a starting point for the solution of the contracted structure. Analysis of neutron diffraction data from the material heat treated at 150, 200, 250 and 300 °C shows that *Cmmm* symmetry is retained to a good approximation. First, structure factors were extracted from the neutron diffraction data using the Le Bail algorithm[27]. The lattice constants (in the *Cmmm* space group), diffractometer zero, scale factor, background, and profile parameters were refined using this extraction technique before any atomic parameters were varied. The lattice constants and weighted residuals using the Le Bail fit are given in the legend of Fig. 2 and represent the best possible fit using the *Cmmm* space group.

A detailed structural analysis was performed on the samples dehydrated at 150, 200, 250 and 300 °C. Fourier difference maps were used to locate the Sr^{2+} cations in the framework for these cases. Three cation positions are located and refined in these structures. Three-site occupancy constraints are used to satisfy both the overall charge balance as well as the total number of cations as known from the room-temperature structure. Two of the cation sites have relatively low occupancies. One of them is the original Sr^{2+} cation site in the room-temperature structure, and the other is a new site located at the centre of the 8MR, in which case the cation coordinates to the oxygen atoms of the 8MR. The third site is heavily occupied, and is also a new cation position. There is another significant peak observed in the Fourier maps which, owing to its coordination environment, is attributed to residual water still adsorbed in the framework. The oxygen (Ow) occupancy on this site decreases significantly with increasing dehydration temperature, in agreement with thermogravimetric data.

Structure refinement

After identifying these structural changes, we conducted Rietveld refinement[28,29] of the data for the samples dehydrated at 150, 200, 250 and 300 °C. However, owing to the low number of observed diffraction peaks and disorder in the material, soft constraints were necessary throughout the refinement—elimination of these constraints results in divergences in the model. The weight of the bond-angle constraints was set to 10% of the weight of the bond-distance constraints, and results in physically realistic bond distances and bond angles. Tables 1a, 1b, 1c and 1d in the Supplementary Information show the refined cation and framework structural parameters. The lattice constants obtained from the Le Bail fit are further refined, with only minor changes occurring in their values. Figures 1a, 1b, 1c and 1d in Supplementary Information show the fitted neutron diffraction patterns for the cases considered here. The fits are reasonably good, and are close to the best possible values in the *Cmmm* space group, as obtained by the Le Bail profile fit.

Received 24 November 2000; accepted 21 June 2001.

1. Hammonds, K. D., Heine, V. & Dove, M. T. Rigid-unit modes and the quantitative determination of the flexibility possessed by zeolite frameworks. *J. Phys. Chem. B* **102,** 1759–1767 (1998).
2. Mentzen, B. F. & Gelin, P. The silicalite p-xylene system. 1. Flexibility of the MFI framework and sorption mechanism observed during p-xylene pore-filling by X-ray powder diffraction at room temperature. *Mater. Res. Bull.* **30,** 373–380 (1995).
3. Nenoff, T. M. *et al.* Flexibility of the zeolite RHO framework. In situ X-ray and neutron powder structural characterization of cation exchanged BePO and BeAsO RHO analogs. *J. Phys. Chem.* **102,** 14256–14264 (1996).
4. Johnson, G. M. *et al.* Flexibility and cation distribution upon lithium exchange of aluminosilicate and aluminogermanate materials with RHO topologies. *Chem. Mater.* **11,** 2780–2787 (1999).
5. Kuznicki, S. M. Large-pored crystalline titanium molecular sieve zeolites. US Patent No. 4853202 (1989).
6. Kuznicki, S. M. & Thrush, K. A. Large-pored molecular sieves with charged octahedral titanium and charged tetrahedral aluminum sites. US Patent No. 5244650 (1993).
7. Kuznicki, S. M. & Thrush, K. A. Large-pored molecular sieves containing at least one octahedral site comprising titanium and at least silicon as a tetrahedral site. US Patent No. 5208006 (1993).
8. Kuznicki, S. M. Preparation of small-pored crystalline titanium molecular sieve zeolites. US Patent No. 4938939 (1990).
9. Anderson, M. W. *et al.* Structure of the microporous titanosilicate ETS-10. *Nature* **367,** 347–351 (1994).
10. Anderson, M. W. *et al.* Microporous titanosilicate ETS-10, a structural survey. *Phil. Mag. B* **71,** 813–841 (1995).
11. Wang, X. & Jacobson, A. J. Crystal structure of the microporous titanosilicate ETS-10 refined from single crystal X-ray diffraction data. *Chem. Commun.* 973–974 (1999).
12. Anderson, M. W. *et al.* Isomorphous substitution in the microporous titanosilicate ETS-10. *Microporous Mater.* **6,** 195–204 (1996).
13. Eldewik, A., Luca, V., Singh, N. K. & Howe, R. F. Iron substitution in the microporous titanosilicate ETS-10. *Proc. Int. Zeolite Conf.* **3,** 1507–1514 (1998).
14. Lamberti, C. Electron-hole reduced effective mass in monoatomic –OTiOTiO– quantum wires embedded in the siliceous crystalline matrix of ETS-10. *Microporous Mesoporous Mater.* **30,** 155–163 (1999).
15. Rocha, J. & Anderson, M. W. Microporous titanosilicates and other novel mixed octahedral-tetrahedral framework oxides. *Eur. J. Inorg. Chem.* 801–818 (2000).
16. Bordiga, S. *et al.* Stoichiometric and sodium-doped titanium silicate molecular sieve containing atomically defined -OTiOTiO- chains: Quantum ab initio calculations, spectroscopic properties, and reactivity. *J. Chem. Phys.* **112,** 3859–3867 (2000).
17. Kuznicki, S. M., Bell, V. A., Petrovic, I. & Desai, B. T. Small-pored crystalline titanium molecular sieve zeolites and their use in gas separation processes. US Patent No. 6068682 (2000).
18. Sandomirskii, P. A. & Belov, N. V. The OD structure of zorite. *Sov. Phys. Crystallogr.* **24,** 686–693 (1979).
19. Mer'kov, A. N. *et al.* Raite and zorite, new minerals from the Lovozero tundra. *Zap. Vses. Mineral. Obshchest.* **102,** 54–62 (1973).
20. Philippou, A. & Anderson, M. W. Structural investigation of ETS-4. *Zeolites* **16,** 98–107 (1996).
21. Braunbarth, C. *et al.* Structure of strontium ion exchanged ETS-4 microporous molecular sieves. *Chem. Mater.* **12,** 1857–1865 (2000).
22. McCusker, L. B. in *Comprehensive Supramolecular Chemistry, Solid-State Supramolecular Chemistry: Two- and Three- Dimensional Inorganic Networks* (eds Alberti, G. & Bein, T.) 393–423 (Pergamon, New York, 1996).
23. Cruciani, G., De Luca, P., Nastro, A. & Pattison, P. Rietveld refinement of the zorite structure of ETS-4 molecular sieves. *Microporous Mesoporous Mater.* **21,** 143–153 (1998).
24. Bieniok, A. & Hammonds, K. D. Rigid unit modes and the phase transition and structural distortions of zeolite rho. *Microporous Mesoporous Mater.* **25,** 193–200 (1998).
25. Bieniok, A. & Baur, W. H. A large volume contraction accompanies the low- to high- temperature transition of zeolite Sr-RHO. *J. Solid State Chem.* **90,** 173–182 (1991).
26. Depmeier, W. in *Molecular Sieves* Vol. 2, *Structures and Structure Determination* (eds Karge, H. J. & Weitkamp, J.) 113–140 (Springer, Berlin, 1999).
27. Le Bail, A., Duroy, H. & Fourquet, J. L. Ab-initio structure determination of $LiSbWO_6$ by X-ray powder diffraction. *Mater. Res. Bull.* **23,** 447–452 (1988).

28. Young, R. A. (ed.) *The Rietveld Method* (Oxford Univ. Press, Oxford, 1993).
29. Larson, A. C. & von Dreele, R. B. *GSAS Report LAUR 86-784* (Los Alamos National Laboratory, 1986).
30. Breck, D. W. *Zeolite Molecular Sieves* (Wiley, New York, 1974).
31. Mitariten, M. & Dolan, W. Nitrogen removal from natural gas with molecular gate technology. *Proc. Laurance Reid Gas Cond. Conf.* **51,** 1–16 (2001).
32. Abrams, L. & Corbin, D. R. in *Topics in Inclusion Science* Vol. 6, *Inclusion Chemistry with Zeolites: Nanoscale Materials by Design* (eds Herron, N. & Corbin, D. R.) 4–6 (Kluwer, Dordrecht, 1995).

Supplementary information is available on *Nature*'s World-Wide Web site (http://www.nature.com) or as paper copy from the London editorial office of *Nature*.

Acknowledgements

We thank J. Curran for discussions and assistance in the preparation of the manuscript, and VTI Corp. for the data of Fig. 5. This work was supported by ATP/NIST, the David and Lucile Packard Foundation and NSF-CTS.

Correspondence and requests for materials should be addressed to S.M.K. (e-mail: steve.kuznicki@engelhard.com).

The timing of the last deglaciation in North Atlantic climate records

Claire Waelbroeck*, Jean-Claude Duplessy*, Elisabeth Michel*, Laurent Labeyrie*†, Didier Paillard* & Josette Duprat‡

** Laboratoire des Sciences du Climat et de l'Environnement, Domaine du CNRS, bât. 12, 91198 Gif-sur-Yvette, France*
† Département des Sciences de la Terre, Université Paris-sud Orsay, bât. 504, 91104 Orsay, France
‡ Département de Géologie et Océanographie, CNRS UMR 5805, Université de Bordeaux I, Talence, France

To determine the mechanisms governing the last deglaciation and the sequence of events that lead to deglaciation, it is important to obtain a temporal framework that applies to both continental and marine climate records. Radiocarbon dating has been widely used to derive calendar dates for marine sediments, but it rests on the assumption that the 'apparent age' of surface water (the age of surface water relative to the atmosphere) has remained constant over time[1,2]. Here we present new evidence for variation in the apparent age of surface water (or reservoir age) in the North Atlantic ocean north of 40° N over the past 20,000 years. In two cores we found apparent surface-water ages to be larger than those of today by 1,230 ± 600 and 1,940 ± 750 years at the end of the Heinrich 1 surge event (15,000 years BP) and by 820 ± 430 to 1,010 ± 340 years at the end of the Younger Dryas cold episode. During the warm Bølling–Allerød period, between these two periods of large reservoir ages, apparent surface-water ages were comparable to present values. Our results allow us to reconcile the chronologies from ice cores and the North Atlantic marine records over the entire deglaciation period. Moreover, the data imply that marine carbon dates from the North Atlantic north of 40° N will need to be corrected for these highly variable effects.

The last deglaciation is a period particularly well dated because it belongs to the time span covered by isotopic (^{14}C) dating techniques, which can be applied to both continental and marine sediments. Moreover, ^{14}C dates can be converted into calendar ages through calibration curves describing the variations in the atmospheric $^{14}C/^{12}C$ ratio over the past 20 kyr (ref. 3). Also, the uncertainty on the absolute dating by annual-layer counting of the Greenland ice cores is small (<550 yr) over the last 15 kyr (ref. 4). Therefore, it is possible to compare directly the timing of events from continental and ice-core records, and thus to infer causal mechanisms from the data. The situation is more complex for the marine data, as the ^{14}C dates are measured on foraminifera preserved in the sediments and hence reflect the $^{14}C/^{12}C$ ratio of the water in which the foraminifera calcified. The surface-water $^{14}C/^{12}C$ ratio is different from that of the contemporaneous atmosphere, reflecting the balance between the input of atmospheric ^{14}C and its removal by transport and radiodecay in the water column. This difference in $^{14}C/^{12}C$ ratio is usually expressed as the apparent or reservoir age of the water mass.

A compilation of pre-bomb surface-water ^{14}C content indicates that the modern surface reservoir age is about 400 ± 100 yr in the tropics and in the North Atlantic whereas it rises to 1,200 yr at higher latitudes in the Southern and North Pacific oceans[5,6]. Past reservoir ages most probably differed from those of today, but only sparse data exist. Reservoir ages have been measured in a few sites at given times in the past, by dating contemporaneous samples in marine sediments and in terrestrial organic matter, marked by the same volcanic ash layer[7–10].

Here, we present summer sea surface temperature (SST) reconstructions and benthic oxygen isotopic records ($\delta^{18}O_b$) from three sediment cores raised for the North Atlantic Ocean between 37 and 55° N (SU 81-18, 37° 46′ N, 10° 11′ W, 3,135 m; CH 69-09, 41° 45′ N, 47° 21′ W, 4,100 m; and NA 87-22, 55° 29′ N, 14° 41′ W, 2,161 m). These records have been dated by accelerator mass spectrometry on monospecific planktonic foraminifera samples[1,11,12] (see Supplementary Information Table 1). Radiocarbon ages have been converted into calendar ages with the CALIB 4.1 software[13], the smoothed (310-yr moving average) 1998 marine calibration curve

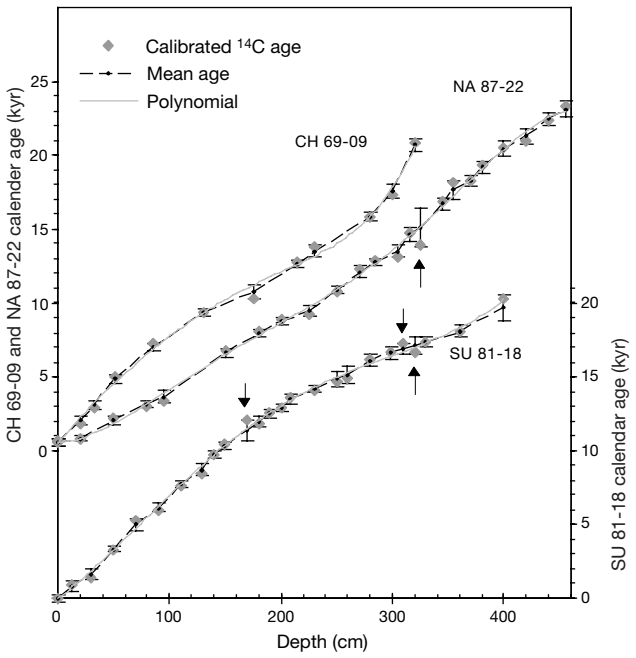

Figure 1 Age–depth relationships for the three North Atlantic deep sea cores. Calendar ages were calculated from the measured ^{14}C ages (see Supplementary Information Table 1) with the CALIB 4.1 software[13] and a constant surface reservoir age of 400 yr. For each core, two different interpolation schemes were used: first, we computed the fifth-order polynomial fitting the dated levels (grey line); second, we linearly interpolated the dated levels, leaving out one age in core NA 87-22 and three ages in core SU 81-18 that showed small age inversions (arrows). The error on the linearly interpolated age scale is taken as one standard deviation of the sample's calendar-age probability distribution given by CALIB 4.1. The error on the polynomial age scale is taken as the difference between the actual sample calendar age and the polynomial age computed at the same level, when this difference is larger than the error on the sample's calendar age. It is otherwise equal to the error on the linearly interpolated age scale. We derived the final age model for each core (black dots with 1-s.d. error bars) by taking the arithmetical mean of the above two timescales to ensure realistically large error bars. The final error estimate includes an additional 200-yr uncertainty, representing the maximum possible bioturbation bias. Both interpolation schemes support our conclusions.